Stratification Breakdown in Antarctic Coastal Polynyas. Part I: Influence of Physical Factors on the Destratification Time Scale

YILANG XU,[a,b] WEIFENG (GORDON) ZHANG,[a] TED MAKSYM,[a] RUBAO JI,[c] AND YUN LI[d]

[a] *Applied Ocean Physics and Engineering Department, Woods Hole Oceanographic Institution, Woods Hole, Massachusetts*
[b] *MIT-WHOI Joint Program in Oceanography/Applied Ocean Science and Engineering, Cambridge, Massachusetts*
[c] *Biology Department, Woods Hole Oceanographic Institution, Woods Hole, Massachusetts*
[d] *School of Marine Science and Policy, University of Delaware, Lewes, Delaware*

(Manuscript received 21 October 2022, in final form 10 June 2023, accepted 14 June 2023)

ABSTRACT: This study examines the process of water-column stratification breakdown in Antarctic coastal polynyas adjacent to an ice shelf with a cavity underneath. This first part of a two-part sequence seeks to quantify the influence of offshore katabatic winds, alongshore winds, air temperature, and initial ambient stratification on the time scales of polynya destratification through combining process-oriented numerical simulations and analytical scaling. In particular, the often-neglected influence of wind-driven circulation on the lateral transport of the water formed at the polynya surface—which we call Polynya Source Water (PSW)—is systematically examined here. First, an ice shelf–sea ice–ocean coupled numerical model is adapted to simulate the process of PSW formation in polynyas of various configurations. The simulations highlight that (i) before reaching the bottom, majority of the PSW is actually carried away from the polynya by katabatic wind–induced offshore outflow, diminishing water-column mixing in the polynya and intrusion of the PSW into the neighboring ice shelf cavity, and (ii) alongshore coastal easterly winds, through inducing onshore Ekman transport, reduce offshore loss of the PSW and enhance polynya mixing and PSW intrusion into the cavity. Second, an analytical scaling of the destratification time scale is derived based on fundamental physical principles to quantitatively synthesize the influence of the physical factors, which is then verified by independent numerical sensitivity simulations. This work provides insights into the mechanisms that drive temporal and cross-polynya variations in stratification and PSW formation in Antarctic coastal polynyas, and establishes a framework for studying differences among the polynyas in the ocean.

KEYWORDS: Antarctica; Sea ice; Coastal flows; Convection; Oceanic mixed layer; Numerical analysis/modeling

1. Introduction

Polynyas, areas of persistent open water surrounded by sea ice, are ubiquitous along the coast of Antarctica (Arrigo and van Dijken 2003) and key components of the Antarctic marine system (Smith and Barber 2007). Antarctic coastal polynyas are often formed by strong offshore katabatic winds with wind speed ≥ 25 m s^{-1} (Rusciano et al. 2013). The enhanced sea ice formation and brine rejection produce saline Dense Shelf Water (DSW), which sinks in the polynya water column, causing substantial vertical mixing (Morales Maqueda et al. 2004). Deepening of the mixed layer in winter brings the nutrient-rich deep water to the surface layer, stimulating biological production in subsequent warmer seasons (Li et al. 2016). If the deepened mixed layer reaches the bottom within the winter months, DSW could flow offshore into the abyssal ocean forming Antarctic Bottom Water (AABW) (Kitade et al. 2014; Ohshima et al. 2013). These physical and biological processes depend highly on the extent of winter mixing in the polynyas (Aoki et al. 2020; Li et al. 2016). Therefore, it is important to determine the wintertime mixing intensity and destratification time scale in the polynyas.

Coastal polynyas around Antarctica vary substantially in terms of their duration of opening, rate of DSW formation, mixing strength, and AABW export. For instance, AABW forms in the Cape Darnley, Mertz, and Ross Sea Polynyas (Ohshima et al. 2013; Williams et al. 2010; Jacobs et al. 1970), but not in the Bellingshausen Sea and Amundsen Sea Polynyas (Schmidtko et al. 2014; Silvano et al. 2018). This difference could result from variations in either shelf physical conditions or dense water sources. DSW formation in polynyas depends on local factors such as atmospheric forcings, sea ice productivity, and strength of ocean stratification (Ohshima et al. 2013; Silvano et al. 2018; Williams and Bindoff 2003). To evaluate the influence of these factors on polynya processes, regional models with realistic configurations are often used (e.g., Mathiot et al. 2012; Nakayama et al. 2017; Schultz et al. 2020). However, this type of model often requires special effort in resolving complex patterns of ice shelf–ocean interactions (Nakayama et al. 2017), sea ice dynamics (Schultz et al. 2020), and katabatic winds (Mathiot et al. 2012).

Idealized models have also been used to investigate the polynya DSW dispersal and impacts of physical factors on the dispersal (Årthun et al. 2013; Chapman and Gawarkiewicz 1997; Chapman 1998, 1999; Visbeck et al. 1996; Wilchinsky and Feltham 2008; Zhang and Cenedese 2014). These studies often use a negative surface buoyancy flux (i.e., downward salt flux) over a fixed area to represent polynya brine rejection. They demonstrated that the density gradient between the dense water chimney and the ambient fluid creates a front, which, through thermal-wind balance, generates a geostrophic rim current around the polynya edge. Baroclinic instability of the rim current then develops into eddies, carrying dense

---

Corresponding author: Yilang Xu, yilangxu@mit.edu

DOI: 10.1175/JPO-D-22-0218.1

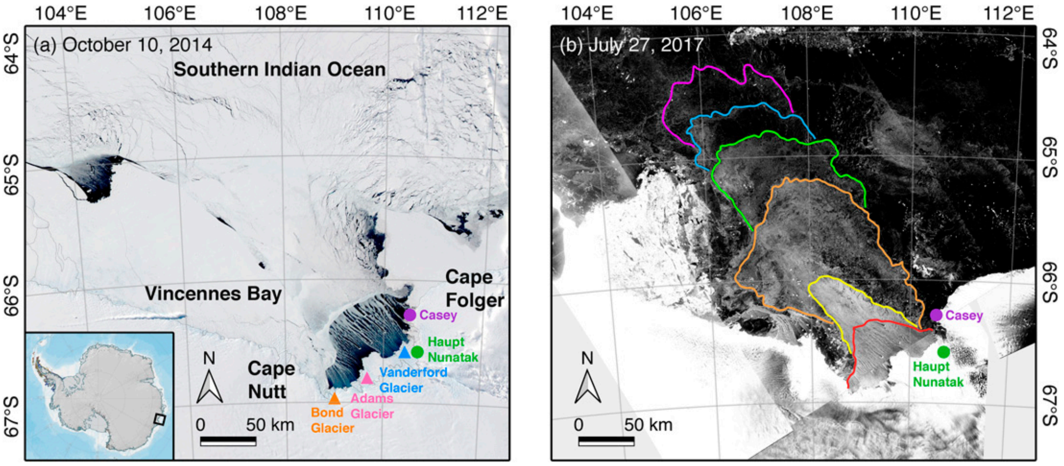

FIG. 1. (a) *Terra*/*Aqua* MODIS satellite image of the Vincennes Bay Polynya on 10 Oct 2014, and (b) Sentinel-1 SAR satellite image of the Vincennes Bay Polynya on 27 Jul 2017. The triangles in (a) locate the nearby glaciers; circles in (a) and (b) denote the locations of Casey and Haupt Nunatak weather stations; colored lines in (b) outline the offshore boundary of the polynya and outer boundaries of the previous sea ice plume. These images are selected to show a clear (cloud-free) pattern of the polynya surface and its offshore sea ice plume in winter.

water away from the polynya (Årthun et al. 2013). Analytical scales of the time and magnitude of dense water downslope propagation have been developed (Chapman 1998; Visbeck et al. 1996). All these idealized numerical and analytical studies were performed in the absence of winds and sea ice. They neglected the momentum exchange among the atmosphere, sea ice and ocean, and the influence of wind-driven circulation. How these factors affect the polynya dynamics remains unknown.

This study seeks to systematically diagnose the influence of a number of physical factors, including winds, air temperature, initial stratification, ice tongue, and coastal geometry on the dispersal of the water mass formed at the polynya surface, which we named Polynya Source Water (PSW) for the purpose of this paper. Note that DSW is part of the PSW that is dense enough to sink to the bottom, while the remaining portion is diluted on its way down by the ambient water and gradually loses its density anomaly in the water column. The Vincennes Bay Polynya (VBP; Fig. 1a) and Terra Nova Bay Polynya (TNBP) are used to illustrate the general pattern of polynya circulation and guide the design of idealized models that are applicable to other polynyas on the Antarctic coast. The VBP is used in Part I to highlight the importance of katabatic winds, while the TNBP is used in Part II (Xu et al. 2023, hereafter Part II) to demonstrate the influence of an ice tongue and a headland.

The VBP is located in the Indian Ocean sector of the Antarctic coast, between Cape Nutt and Cape Folger. In winter, strong katabatic winds are channeled into the Vanderford, Adams, and Bond Glaciers, blow offshore (northwestward), and extend beyond the Vincennes Bay (Nihashi and Ohshima 2015; Parish and Bromwich 2007), forming the VBP. Data from the nearby Casey and Haupt Nunatak weather stations (Barnes-Keoghan 2000) show intensification of winds during 2017 winter (May–September) when the air temperature frequently drops below −20°C (Figs. 2a,b). The katabatic winds are mainly offshore (Figs. 2d,e), particularly at the Haupt Nunatak station, close to the center of the polynya (Fig. 1). Spectra of the wind speed show strong oscillations in the period band of 2–5 days (Fig. 2c). Besides the offshore winds, alongshore easterly winds are also present (Fig. 2d). These conditions of offshore and coastal easterly winds are common to Antarctic coastal polynyas (e.g., Mathiot et al. 2010; Nihashi and Ohshima 2015).

Wintertime katabatic winds at the VBP are accompanied by enhanced offshore sea ice export, as indicated by the offshore-flowing sea ice plume in the Sentinel-1 SAR satellite image (Fig. 1b). Similar sea ice plumes have been reported in other Antarctic coastal polynyas, including the Ross Sea Polynya, and the bright–dark bands in the plumes represent episodic export of sea ice induced by katabatic wind events (Dai et al. 2020). Overall, the VBP has a medium sea ice production rate ($73.3 \pm 9.9\ \mathrm{km^3\ yr^{-1}}$) among the major Antarctic coastal polynyas (30–$400\ \mathrm{km^3\ yr^{-1}}$; Tamura et al. 2008). It forms DSW that flows offshore supplying the AABW (Kitade et al. 2014). The process of DSW formation and water column destratification in the VBP is captured by temperature and salinity profiles from instrumented elephant seals (Roquet et al. 2014, 2021). For example, during April 2012 (early winter), the water column in the VBP is stratified (Fig. 3). The mean salinity difference between the surface and bottom layers is ~0.4 psu and the mean density difference is $\sim 0.3\ \mathrm{kg\ m^{-3}}$. Note that temperature changes in the region have negligible influence on density, and salinity changes completely dominate the density variation. By the end of the winter (September 2012), the polynya water column is completely mixed. It thus took less than 5 months to break down the water column stratification in this case.

Here we hypothesize that the strength of wintertime vertical mixing and the time required to break down the water

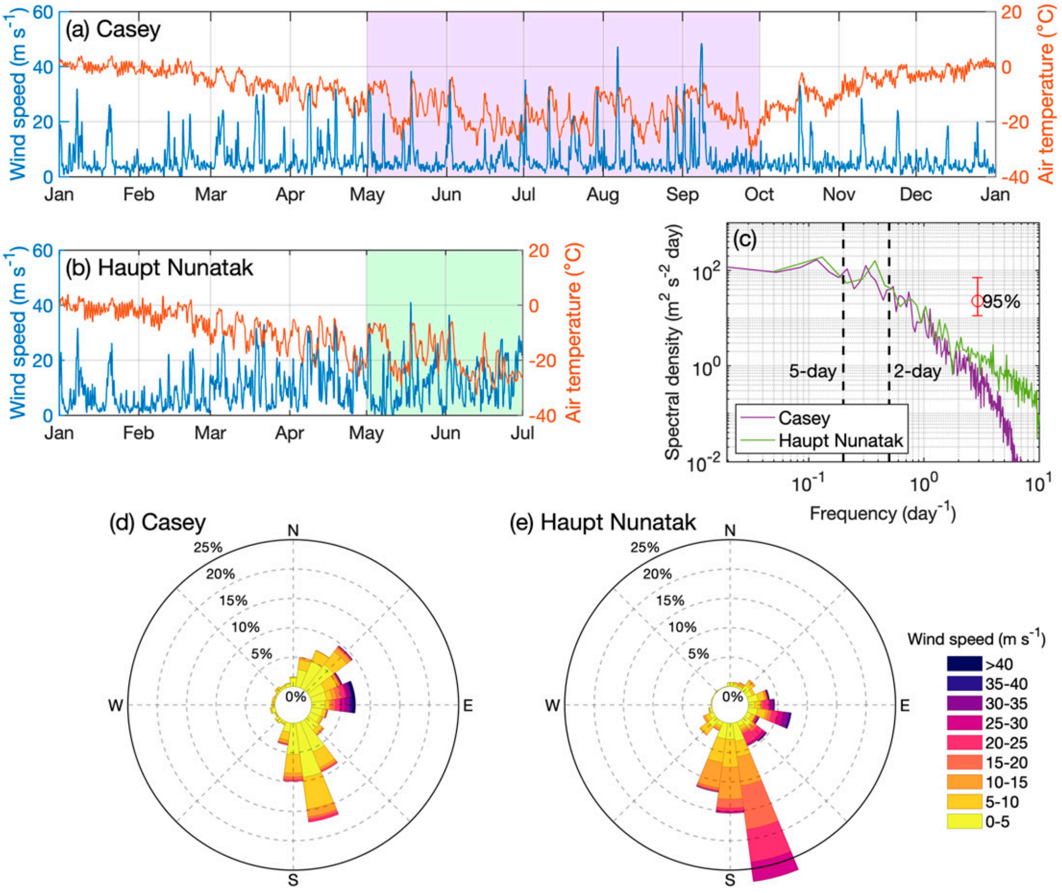

FIG. 2. Wind speed and air temperature measured at the (a) Casey and (b) Haupt Nunatak weather stations in 2017; (c) spectral density of the measured wind speed; (d),(e) wind rose plots of the wind speed and the direction it comes from in the winter months (May–September). Note that the Haupt Nunatak station is closer to the center of the polynya, but no data are available there for the second half of 2017. The purple and green shades in (a) and (b) highlight the austral winter months; the error bar in (c) indicates the 95% confidence interval; dashed lines in (c) denote frequencies corresponding to wind periods of 2 and 5 days.

column stratification in coastal polynyas are affected by polynya circulation. Both winds and coastal geometry (e.g., ice tongues and headlands) can modify three-dimensional polynya flows and potentially affect the lateral dispersal of the water mass formed by buoyancy loss at the polynya surface. Therefore, the process of polynya mixing is likely a three-dimensional process, rather than a one-dimensional (vertical) process that is often assumed by previous studies. Focusing on the impact of the wind-driven circulation on polynya mixing, Part I of this study uses an ice shelf–sea ice–ocean coupled numerical model to simulate idealized Antarctic coastal polynyas and investigate the water-column destratification time scale. The impact of polynya circulation induced by complex coastal geometry will be studied in Part II.

2. Numerical model

a. Model setup

The Massachusetts Institute of Technology General Circulation Model (MITgcm; Marshall et al. 1997) with coupled ice shelf, sea ice (Losch 2008; Losch et al. 2010), and ocean modules is used here. MITgcm has been used in various Antarctic coastal studies (Nakayama et al. 2017, 2019; Schultz et al. 2020). We use an idealized setup to capture fundamental processes in a wide range of Antarctic coastal polynyas. The model uses a spherical polar coordinate and covers a region of 22.5° in longitude (0°–22.5°E) and 6° in latitude (77°–71°S) with a uniform water depth h_N (Fig. 4). Note that the absolute values of the coordinates in this process-oriented idealized study are used for convenience, similar to previous studies (e.g., Årthun et al. 2013; Wilchinsky and Feltham 2008), and the model result does not change with coordinates within the range of Antarctica coastal polynyas (section 4). The southern boundary of the domain is on the land, which is incised by an ice shelf (see below), while the other three boundaries are open in the ocean. The horizontal grid spacing is ~1 km in the central study area and gradually increases toward the open boundaries (Fig. 4a). Because the Rossby deformation radius in the Antarctic coastal region is ~5 km, a horizontal grid spacing of 1 km or less is required to resolve baroclinic

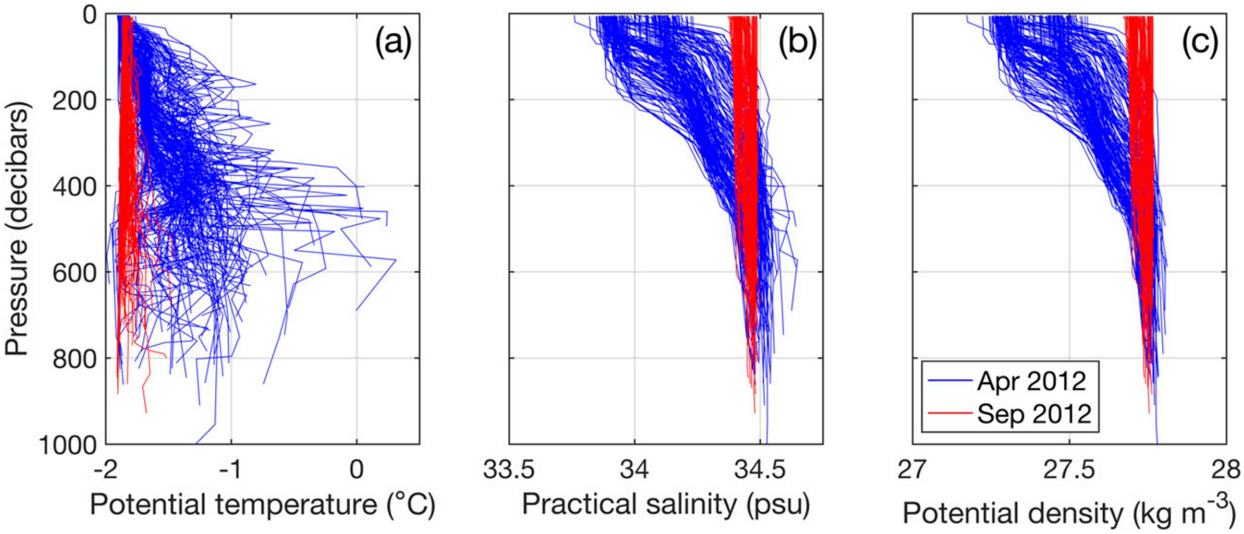

FIG. 3. (a) Potential temperature, (b) practical salinity, and (c) potential density profiles recorded by instrumented elephant seals in the Vincennes Bay Polynya over 109°–110°E, 66°–67°S in April (early winter) and September (late winter) 2012.

eddies associated with the PSW dispersal (Årthun et al. 2013). The model vertical grid is uniformly spaced with a layer thickness of 10 m. Note that at ~1-km horizontal resolution, modeled characteristics of PSW transport are similar between hydrostatic and nonhydrostatic simulations (Årthun et al. 2013). This is consistent with the fact that the nonhydrostatic convection induced by the brine rejection occurs over a much smaller horizontal scale and thus cannot be explicitly resolved by any models at this resolution. Hence, the hydrostatic approximation is used here for faster computations, and the implication will be discussed in section 5.

A rectangular ice shelf, located between 10.3° and 12.3°E and between 77° and 76°S, is sandwiched by land on both sides, and its offshore end aligns with the ambient coastline. The cross-sectional shape of the ice shelf follows those in Årthun et al. (2013) and Losch (2008) with ice thickness decreasing gradually northward from the maximum value of 400 m on the southern end to 0 on the northern edge. The vertical profile of the ice shelf front is smoothened to improve numerical stability and its wedge shape forms a cavity underneath. The katabatic winds blow northward off the ice shelf front. To mimic the katabatic wind patterns in the Antarctic Mesoscale Prediction System as analyzed by Guest (2021a) and Wenta and Cassano (2020), the wind field specified in this study has a half-elliptic shape with the highest speed in the central region between 10.3° and 12.3°E and between 76° and 75°S, and it linearly decays outward to 0 in a region of ~55 km wide (Fig. 4b). Based on the winds measured near coastal polynyas around Antarctica (e.g., Adolphs and Wendler 1995; Knuth and Cassano 2011; Wendler et al. 1997) and the wind data presented in Fig. 2, the katabatic wind speed at 10-m height, V_{wind}, is assumed to oscillate with time t following the form,

$$V_{\text{wind}} = V_a\left(1 - \cos\frac{2\pi t}{P_{\text{wind}}}\right), \qquad (1)$$

where P_{wind} is the wind oscillation period and V_a is the time-averaged wind speed. Within an oscillation period, V_{wind} varies between 0 and $2V_a$.

To include the effect of coastal easterly winds that are ubiquitous along the Antarctic coast, in some of the simulations, westward winds with speed U_a are prescribed over most of the domain. The U_a linearly decreases to 0 within a ~80–110-km-wide ramping zone adjacent to the open boundaries. For simplicity, only steady alongshore wind speed is considered here. Additional simulations with oscillating alongshore winds suggest that oscillations in alongshore winds do not change the general dispersal pattern of the water mass formed at the polynya surface (not shown).

The sea ice module (Losch et al. 2010) used is based on the viscous-plastic dynamic–thermodynamic sea ice model proposed by Zhang and Hibler (1997). Sea ice parameters are adapted from the LLC4320 simulation (Rocha et al. 2016) with the following modifications. The sea ice is discretized into 7 thickness categories, and the subgrid-scale ice thickness distribution scheme is used, which follows the probability density function proposed by Thorndike et al. (1975) and the participation and ridging function in Lipscomb et al. (2007). Sea ice strength changes with its concentration and thickness, and is parameterized following Hibler (1979). Table 1 shows values of the sea ice parameters in MITgcm used in this study. To represent early-winter conditions, the model is initialized with sea ice concentration of 1 (100% of the grid area) and thickness of 0.5 m over the entire domain. To avoid boundary condition issues, sea ice concentration and thickness are set to 0 on all open boundaries. Note that the general pattern of modeled polynyas in the middle of the domain is not sensitive to the sea ice boundary condition. The ice shelf module implemented by Losch (2008) is used to parameterize basal melting under the ice shelf. It uses a three-equation system with a linear turbulent flux formulation (Hellmer and Olbers 1989;

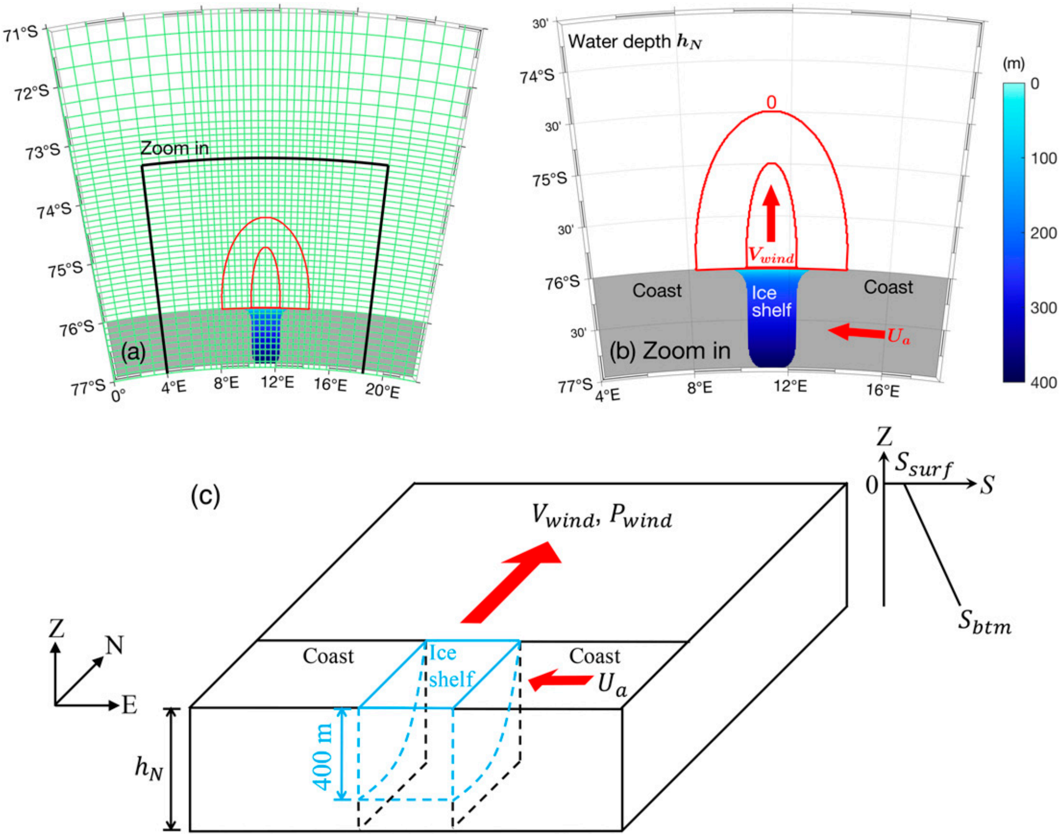

FIG. 4. (a) An aerial view of the model domain and grid and (b) a zoomed-in view of the region marked by black lines in (a). Green lines in (a) depict every 10 horizontal grid cells; the gray regions in (a) and (b) indicate land; the filled color shows the vertical position of the interface between the ice shelf and ocean, i.e., thickness of the ice shelf; red ellipses outline regions of the offshore katabatic wind V_{wind} and its inner region of maximum speed; red arrows in (b) indicate the directions of V_{wind} and the alongshore easterly winds U_a in Run B2; (c) a three-dimensional schematic illustration of the model setup and the initial salinity profile.

Jenkins et al. 2001) to simulate the melting/refreezing-induced mass and heat fluxes across the ice shelf and ocean interface.

To simulate the dispersal of all water mass formed by the buoyancy loss at the polynya surface, a passive tracer is continuously injected into the polynya surface. Following the literature (e.g., Ding et al. 2020; Parmiggiani 2006), the polynya surface in the model is defined as the coastal area within the region of 8°–14.5°E and 76°–75.5°S where sea ice concentration is <70% (leads farther offshore are excluded). At every time step, the polynya region is recomputed according to the modeled sea ice concentration, and surface concentration of the passive tracer in the polynya region is set to 1. Subject to advection, mixing and ice shelf meltwater dilution, the passive tracer spreads out vertically and horizontally, manifesting spreading of the PSW, including the DSW that sinks down to the bottom and the portion that loses its density anomaly and being carried away in the middle of the water column.

TABLE 1. Main sea ice parameters in MITgcm and their values used in this study.

Name	Description	Value
SEAICE_dryIceAlb	Winter sea ice albedo	0.8509
SEAICE_wetIceAlb	Summer sea ice albedo	0.7284
SEAICE_drySnowAlb	Dry snow albedo	0.7754
SEAICE_wetSnowAlb	Wet snow albedo	0.7753
SEAICE_drag	Nondimensional air-ice drag coefficient	0.002
SEAICE_waterDrag	Nondimensional water-ice drag coefficient	0.0055
HO	Demarcation ice thickness	0.2 m

The nonlocal *K*-profile parameterization (KPP; Large et al. 1994) and the Smagorinsky (1963) scheme are used to simulate vertical and horizontal mixing, respectively. The minimum vertical viscosity is set to 10^{-7} m^2 s^{-1}. The KPP background diffusivity is 5×10^{-7} m^2 s^{-1}, as suggested by Nguyen et al. (2011). The KPP scheme computes vertical mixing coefficients in the boundary layers and the interior through parameterizing the impacts of surface forcing, shear instability, internal wave activity, and static instability (Large et al. 1994). Note that model results are not sensitive to the static instability parameterization as test simulations with the static instability factor altered by two orders of magnitude show negligible differences in modeled destratification time scales. The third-order direct-space-time flux limiter

TABLE 2. Sensitivity simulations and the corresponding parameter values. The altered values of the parameters are shown in bold. The target parameter values that are altered for each sensitivity simulation set are further shown in bold italic font. An asterisk (*) indicates a calibration set, and a dagger (†) indicates a validation set. Brackets denote the range of the parameter values.

Sensitivity simulation set	V_a (m s^{-1})	U_a (m s^{-1})	T_a (°C)	S_{btm} (psu)	h_N (m)	P_{wind} (days)
G1-Vwind*	***[12.5, 27.5]***	0	−20	34.25	500	2
G2-Vwind†	***[12.5, 27.5]***	0	**−30**	34.25	500	2
G1-Uwind*	20	***[0, 15]***	−20	34.25	500	2
G2-Uwind†	20	***[0, 15]***	**−30**	34.25	500	2
G1-Tair†	20	0	***[−40, −10]***	34.25	500	2
G2-Tair†	**15**	0	***[−40, −10]***	34.25	500	2
G1-Nini†	20	10	−20	***[34, 34.5]***	500	2
G2-Nini†	20	**15**	−20	***[34, 34.5]***	500	2
G1-Hdepth†	20	10	−20	[34.25, 34.4] (maintain $N = 0.002$ s^{-1})	***[500, 800]***	2
G2-Hdepth†	20	**15**	−20	[34.25, 34.4] (maintain $N = 0.002$ s^{-1})	***[500, 800]***	2
G1-Pwind†	20	0	−20	34.25	500	***[0.5, 5]***
G2-Pwind†	**15**	0	−20	34.25	500	***[0.5, 5]***
G2-Pwindx†	**25**	0	−20	34.25	500	***[0.5, 5]***

advection scheme is applied to salinity, temperature and passive tracer. The coastal and ice shelf boundaries are free-slip, and frictional boundary condition with a quadratic drag coefficient of 2.5×10^{-3} is applied to the ocean bottom and the base of the ice shelf. The Orlanski radiation condition (Orlanski 1976) with preserved model volume is imposed on the lateral open boundaries for ocean temperature, salinity, and velocity.

For the first two base runs (hereinafter referred to as Run B1 and B2), the ocean is initialized with a near-freezing temperature of −1.8°C everywhere, and a linear salinity profile of 34–34.25 psu from the surface to the bottom (at 500 m), both representative of the hydrographic conditions in Antarctic coastal polynyas, such as the VBP (Fig. 3) and TNBP (Le Bel et al. 2021; Rusciano et al. 2013). The corresponding buoyancy frequency N equals 0.002 s^{-1}. Because density variation induced by typical temperature changes in the polynyas is negligible compared to that induced by salinity changes (e.g., Ohshima et al. 2022), using an initially uniform near-freezing temperature in the model does not affect the model dynamics. Meteorological conditions typical to wintertime katabatic wind events in Antarctic coastal polynyas (Guest 2021a,b) with constant downward longwave radiation of 200 W m^{-2}, specific humidity at 2-m height of 5×10^{-4}, and air temperature at 2-m height of $T_a = -20$°C are used. The mean offshore wind speed in Eq. (1) is set as $V_a = 20$ m s^{-1} with $P_{\text{wind}} = 2$ days, representative of the wintertime winds measured at the VBP (Fig. 2). Applying these conditions in the model produces a pattern of heat fluxes qualitatively similar to that observed in the TNBP (see Part II). In Run B1, no alongshore wind is applied, i.e., $U_a = 0$, while in Run B2 steady coastal easterly wind of $U_a = 10$ m s^{-1} is applied. All simulations are integrated for 200 days.

To validate results of the analytical scaling, two groups of sensitivity simulations, G1 and G2, are carried out (Table 2). G1 has six sensitivity sets (G1-Vwind, G1-Uwind, G1-Tair, G1-Nini, G1-Hdepth, and G1-Pwind) designed around Run B1 and B2, corresponding to six sensitivity parameters: mean speed of the offshore winds V_a, alongshore wind speed U_a, air temperature T_a, initial stratification N, water depth h_N, and wind oscillation period P_{wind}. Each of the sensitivity sets consists of a number of simulations with the value of only one target parameter being altered (numbers in italic in Table 2). All other parameters are kept the same as the control values used in B1 and B2 (nonbolded numbers in Table 2). Note that the value of N is modified by changing the initial bottom salinity S_{btm}, while keeping surface salinity, $S_{\text{surf}} = 34$ psu, fixed. Ranges of the parameter values are chosen to represent typical conditions of Antarctic coastal regions. For instance, when $h_N = 500$ m, S_{btm} varies between 34 and 34.5 psu, which gives the bottom-to-surface salinity difference ($S_{\text{btm}} - S_{\text{surf}}$) of 0–0.5 psu, consistent with observations at the VBP (Fig. 3b). Note that when the water depth h_N increases, S_{btm} increases to keep $N = 0.002$ s^{-1} in the entire water column, as in Run B1 and B2. The maximum offshore wind speed $2V_a$ varies between 25 and 55 m s^{-1}, consistent with katabatic wind speed (Rusciano et al. 2013).

The second group of sensitivity simulations G2, is for *independent* validation of the scaling (see below). Each simulation set in G2 differs from the corresponding set in G1 by one parameter. That is, in each G2 simulation, two parameters have values altered from those in the base run. For instance, in the G2-Vwind set, besides altering the value of V_a, T_a is set at −30°C, differing from −20°C in both the base run and the G1-Vwind set. Meanwhile, besides having G2-Pwind with $V_a = 15$ m s^{-1}, an extra set of simulations, G2-Pwindx with $V_a = 25$ m s^{-1}, is added to examine the dependence on the oscillation of winds stronger than that in the base run with $V_a = 20$ m s^{-1}.

Altogether, 63 simulations, categorized into 13 sets, are presented in Part I of this study. Two sensitivity sets in G1, namely, G1-Vwind and G1-Uwind, are used to determine values of the coefficients in the analytically scaled formula through least squares fitting. They are referred to as *calibration* sets. The other 11 sets are referred to as *validation* sets, as the simulations within are independent of the analytical scaling, and they are used to validate the scaled formula.

b. *General pattern of modeled polynyas*

Snapshots of sea ice concentration and thickness, potential density, and passive tracer concentration on model day 100 in

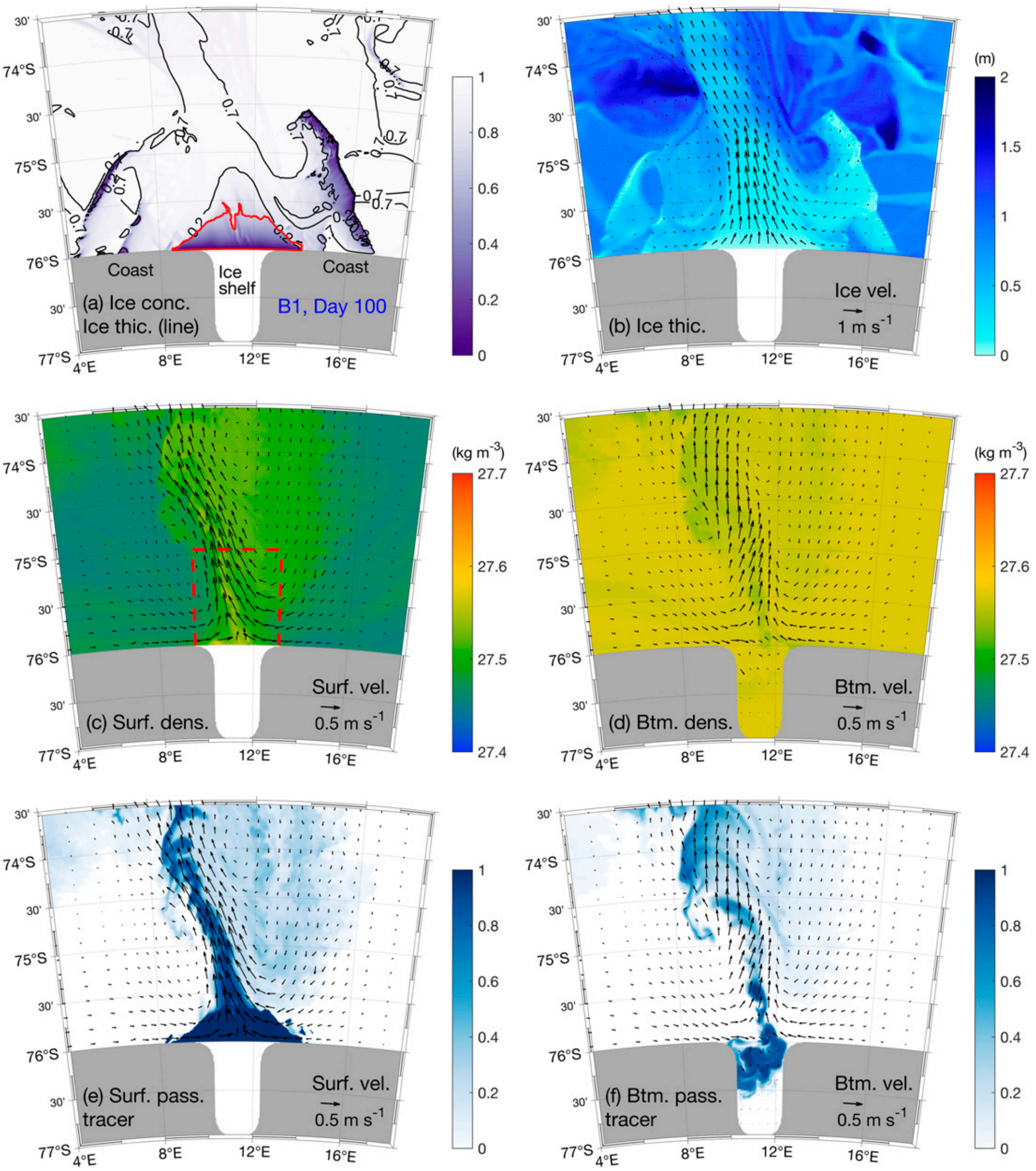

FIG. 5. Snapshots of model fields on day 100 from Run B1: (a) sea ice concentration (color) and thickness (black contours in meters); (b) sea ice thickness (color) and sea ice velocity (arrows); potential density (color) and velocity (arrows) at the (c) surface and (d) bottom; concentration of passive tracer (color) originating from the polynya surface and velocity (arrows) at the (e) surface and (f) bottom. The red line in (a) outlines the coastal polynya on day 100; the red dashed box in (c) indicates the region where modeled fields are averaged zonally and shown in Fig. 7.

both Run B1 and B2 show a coastal polynya forming at the center of the wind field (Figs. 5 and 6). In both simulations, as the winds push the sea ice northward, sea ice thickness gradually increases offshore, constraining further expansion of the polynya. A strong offshore ocean current is formed. At the ocean surface, density increases not only within the polynya, but also in the offshore regions. As indicated by the passive tracer field, PSW formed at the polynya surface is carried away from the polynya by the wind-driven offshore outflow over the water column, as indicated by the surface and bottom distribution. Meanwhile, some of the PSW sinks down to the bottom layer of the polynya water column and flows into the ice shelf cavity to the south of the polynya (Figs. 5f and 6f).

Runs B1 and B2 also show prominent differences. In B1, the sea ice and ocean fields are nearly symmetric between the east and west with a slightly westward shift due to the Coriolis effect (Figs. 5b–d). In contrast, in B2, a strong westward veering is observed in the sea ice and surface ocean velocity fields

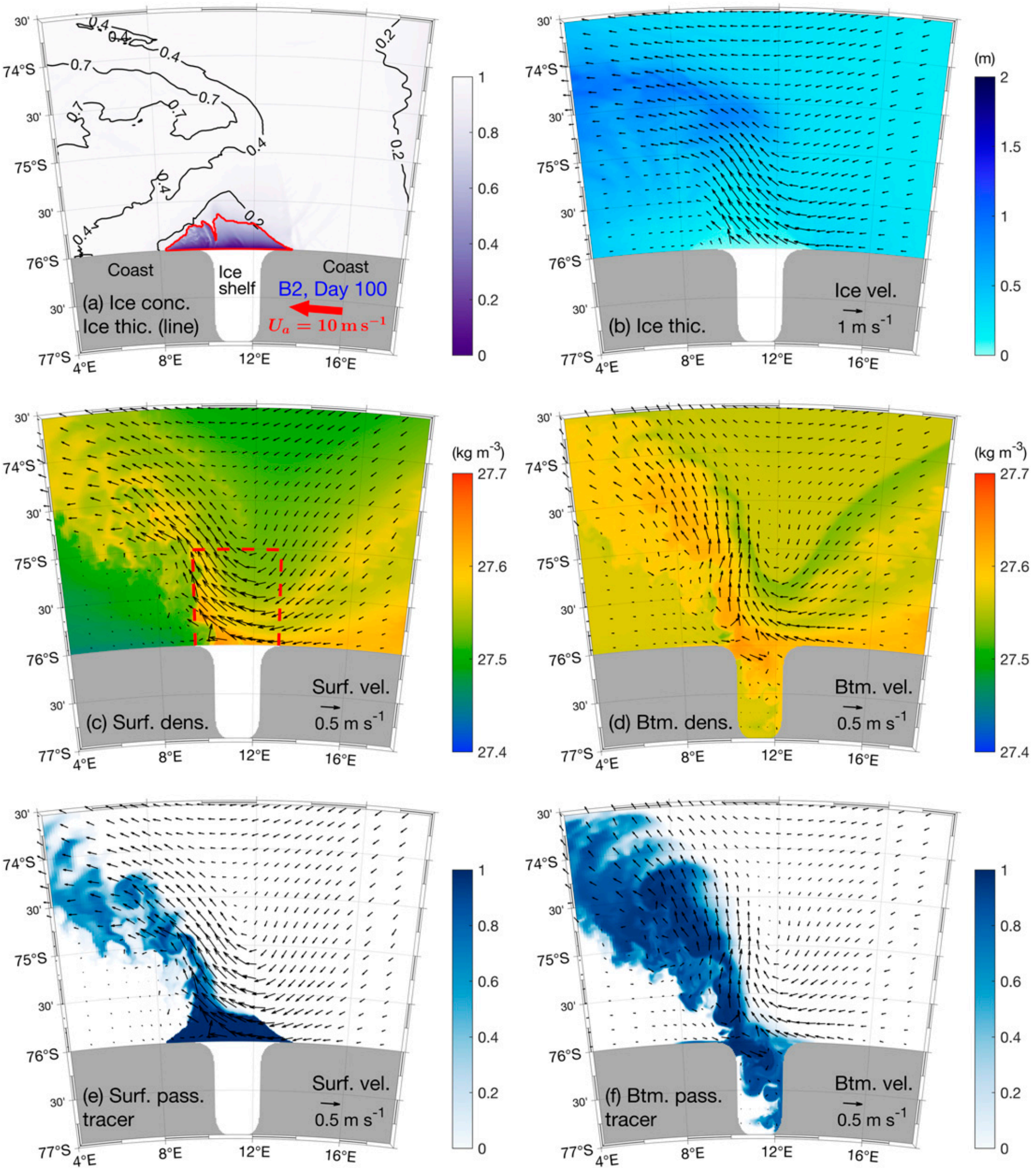

FIG. 6. Snapshots of model fields on day 100 from Run B2: (a) sea ice concentration (color) and thickness (black contours in meters); (b) sea ice thickness (color) and sea ice velocity (arrows); potential density (color) and velocity (arrows) at the (c) surface and (d) bottom; concentration of passive tracer (color) originating from the polynya surface and velocity (arrows) at the (e) surface and (f) bottom. The red line in (a) outlines the coastal polynya on day 100; the red dashed box in (c) indicates the region where modeled fields are averaged zonally and shown in Fig. 7.

(Figs. 6b–d). The maximum bottom density is higher in B2 than B1 (Figs. 5d and 6d). Meanwhile, more PSW has penetrated to the polynya bottom and entered the ice shelf cavity in B2 (Fig. 6f) than B1 (Fig. 5f), indicating faster sinking of PSW in the polynya in B2.

The major difference between circulations in B1 and B2 is that the alongshore winds in B2 drive onshore Ekman transport (Ekman 1905). This is illustrated by differences in cross-shore vertical profiles of potential density and offshore velocity in the simulations (Fig. 7). The model fields here are temporally averaged over days 90–100 and zonally averaged over the polynya region (9.5°–13°E) to eliminate high-frequency and small-scale variations. The comparison shows that Run B2 produces higher density beneath the polynya surface (Fig. 7c) and weaker offshore velocity in the surface 150 m of the polynya water column (Fig. 7f). These are consistent with onshore Ekman transport generated by the coastal easterly winds suppressing the offshore current and diminishing offshore transport of the PSW. Note that Davis and McNider (1997) examined onshore Ekman transport of offshore water induced by

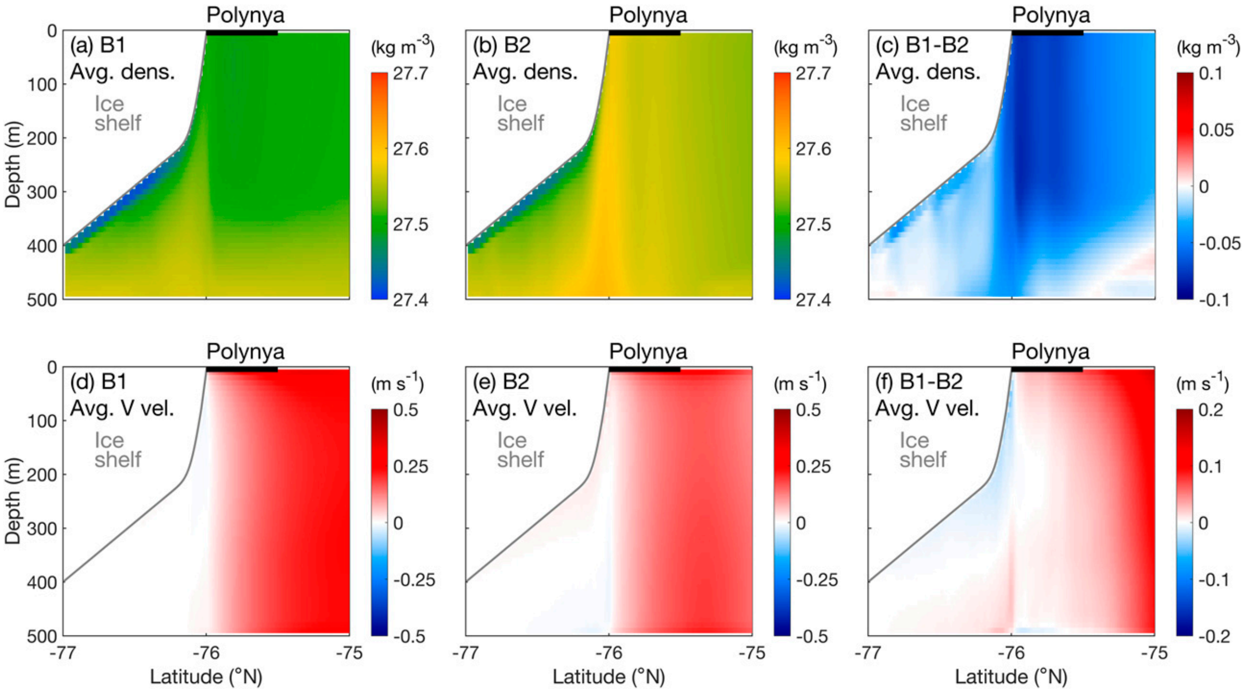

FIG. 7. Cross-shore sections of (top) potential density and (bottom) offshore velocity from Run (left) B1 and (center) B2, and (right) their differences. The plotted fields are temporally averaged over day 90–100 and zonally averaged within the area delineated by the red dashed lines in Figs. 5c and 6c. The black bars on the top of the panels highlight the polynya region.

alongshore easterly winds, but they did not consider the impact of Ekman dynamics on the PSW circulation. It will be quantified in this study.

Snapshots of the model fields along the trajectories of the PSW outflow (red dashed lines in Figs. 8a and 9a) on day 40 in both Runs B1 and B2 show that the wind-driven offshore flow is largely barotropic (Figs. 8d,e and 9d,e) and that the PSW passive tracer occupies much of the water column even offshore of the polynya (Figs. 8b and 9b). The offshore outflow thus carries much of the PSW directly offshore before it can reach the bottom. Quantification of the modeled passive tracer indicated that, by day 100, 93% of the PSW is transported offshore of the polynya in Run B1, and the rest sinks down locally in the polynya region and flows under the ice shelf. Because the onshore Ekman transport driven by the coastal easterly winds in B2 reduces the offshore current in the top 150 m, it suppresses offshore transport of the PSW and allows more PSW to remain in the polynya region. By day 100 only 85% of the polynya PSW is transported offshore of the polynya in B2. Therefore, more PSW is able to stay in the polynya and sink down to the polynya bottom. This is consistent with B2 having (i) stronger polynya convection, as indicated by a higher magnitude of the vertical velocity in the polynya region (Fig. 9f), (ii) more PSW passive tracer in the polynya bottom layer (Fig. 9b), (iii) deeper surface mixed layer (Fig. 9c), and (iv) more PSW flowing into the ice shelf cavity than in B1 (Figs. 5f and 6f). Following other studies of the high-latitude environment (e.g., Dong et al. 2008; Kusahara et al. 2017; Meehl et al. 2019), the surface mixed layer depth (MLD) is defined as the depth where the potential density differs from the surface density by a threshold $\Delta\rho_{\mathrm{MLD}} = 0.05$ kg m^{-3}. Note that this choice of the density difference threshold affects values of the modeled destratification time scale, but not the diagnosis of the dynamical influence of the factors on the time scale or the conclusion of this study.

The modeled horizontal velocities in the ocean in both B1 and B2 being largely barotropic over the 500-m-deep water column is intriguing. It suggests that, despite the great depth, the influence of the ocean surface stress is able to penetrate through the entire water column reaching the bottom. To confirm that, we examine the vertically integrated cross-shore momentum balance, which shows that a nonnegligible portion of the surface stress τ_{sy} is balanced by the bottom stress τ_{by}. Particularly, in Run B1, the mean τ_{sy} in a box to the immediate north of the polynya on days 90–100 is ~1.3 N m^{-2}, and the mean τ_{by} in the same region and time window is ~0.22 N m^{-2} (Fig. 10c). The sensitivity simulations (G1-Vwind) of different offshore wind strength, V_a, show that τ_{by} increases almost linearly with τ_{sy} (Fig. 10c), confirming that the imposed katabatic winds affect the entire water column. The model also shows that the rest of the surface stress is largely balanced by pressure gradient forces associated with sea level tilt and horizontal density gradient. Neglecting the advection, horizontal diffusion, and Coriolis terms, the depth-integrated cross-shore momentum balance in a steady state can be approximated as

$$\tau_{by} \approx \tau_{sy} - \frac{g}{2}\frac{\partial \rho}{\partial y} h_N^2 - g\rho_0 \frac{\partial \eta}{\partial y} h_N . \qquad (2)$$

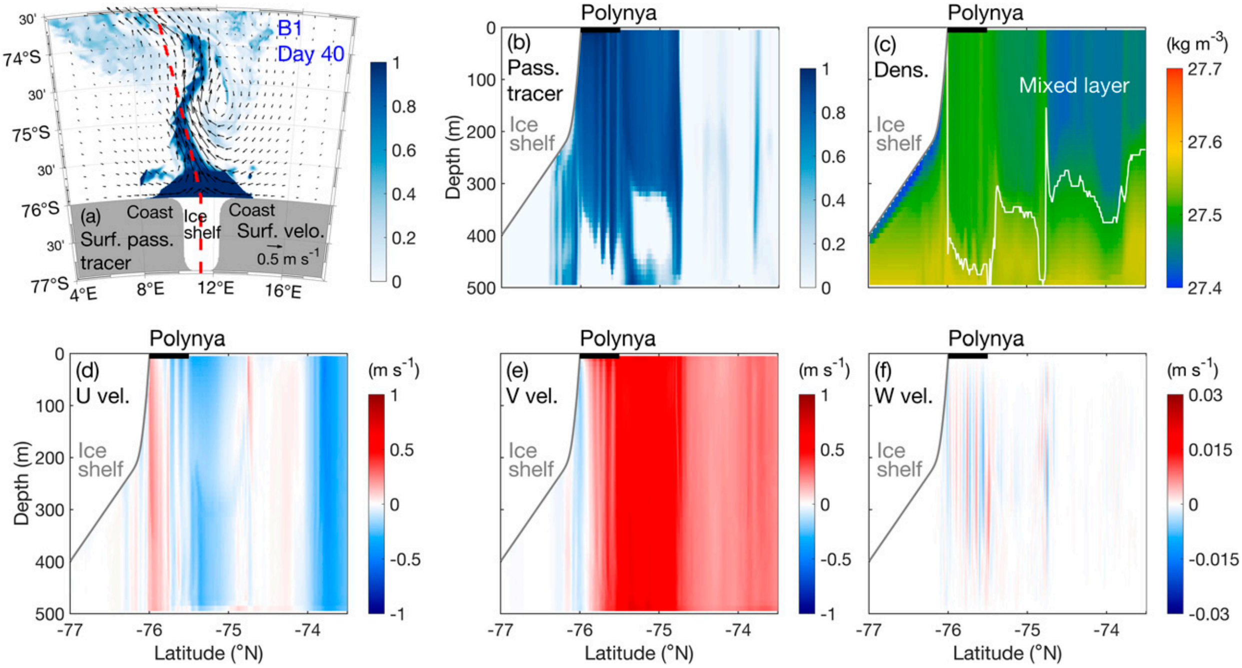

FIG. 8. Snapshots of model fields on day 40 from Run B1: (a) surface concentration of PSW passive tracer (color) and surface velocity (arrow); cross-shore sections of (b) passive tracer, (c) potential density and surface mixed layer depth (white line), (d) zonal velocity, (e) meridional velocity, and (f) vertical velocity along the red dashed line in (a). The black bars in (b)–(f) highlight the polynya region.

Here, $\partial\rho/\partial y$ is the horizontal density gradient, η is the sea surface height and h_N is the water depth, $\rho_0 = 1030$ kg m^{-3} is the reference density of seawater, $g = 9.81$ m s^{-2} is the gravitational acceleration. In (2), $\partial\rho/\partial y$ is assumed to be constant throughout the water column and does not change with water depth. As the water depth increases, the amount of salt staying in the polynya water column presumably increases, which tends to counterbalance change in the mean polynya water

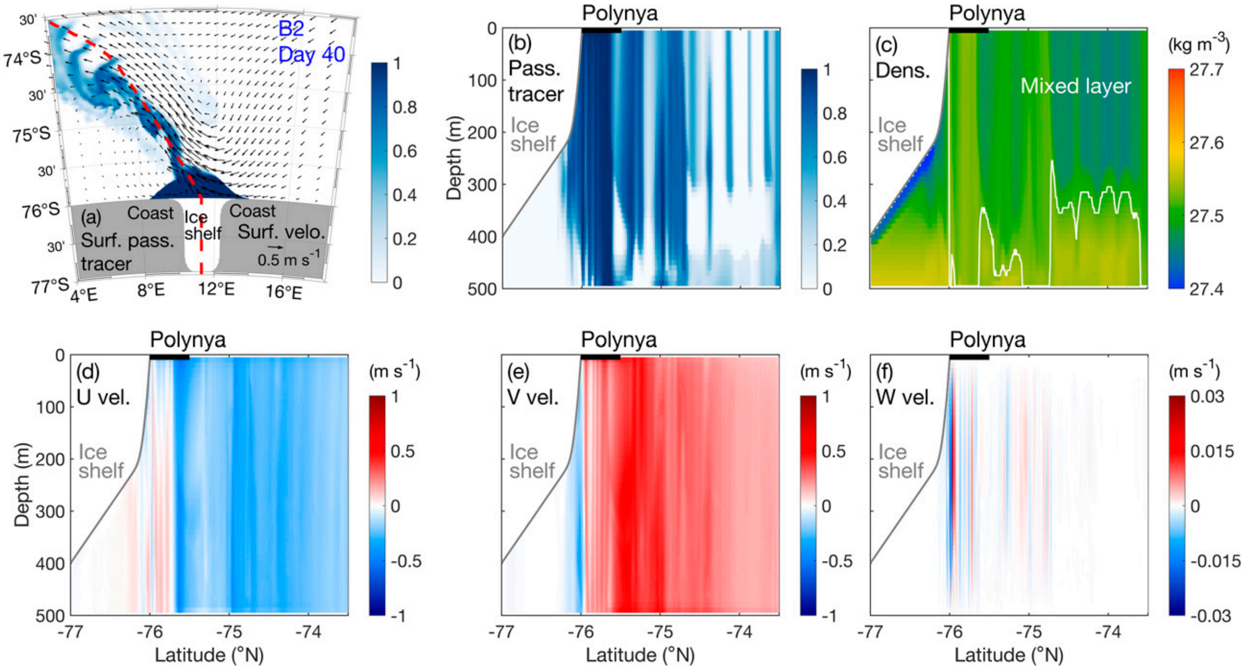

FIG. 9. Snapshots of model fields on day 40 from Run B2: (a) surface concentration of PSW passive tracer (color) and surface velocity (arrow); cross-shore sections of (b) passive tracer, (c) potential density and surface mixed layer depth, (d) zonal velocity, (e) meridional velocity, and (f) vertical velocity along the red dashed line in (a). The black bars in (b)–(f) highlight the polynya region.

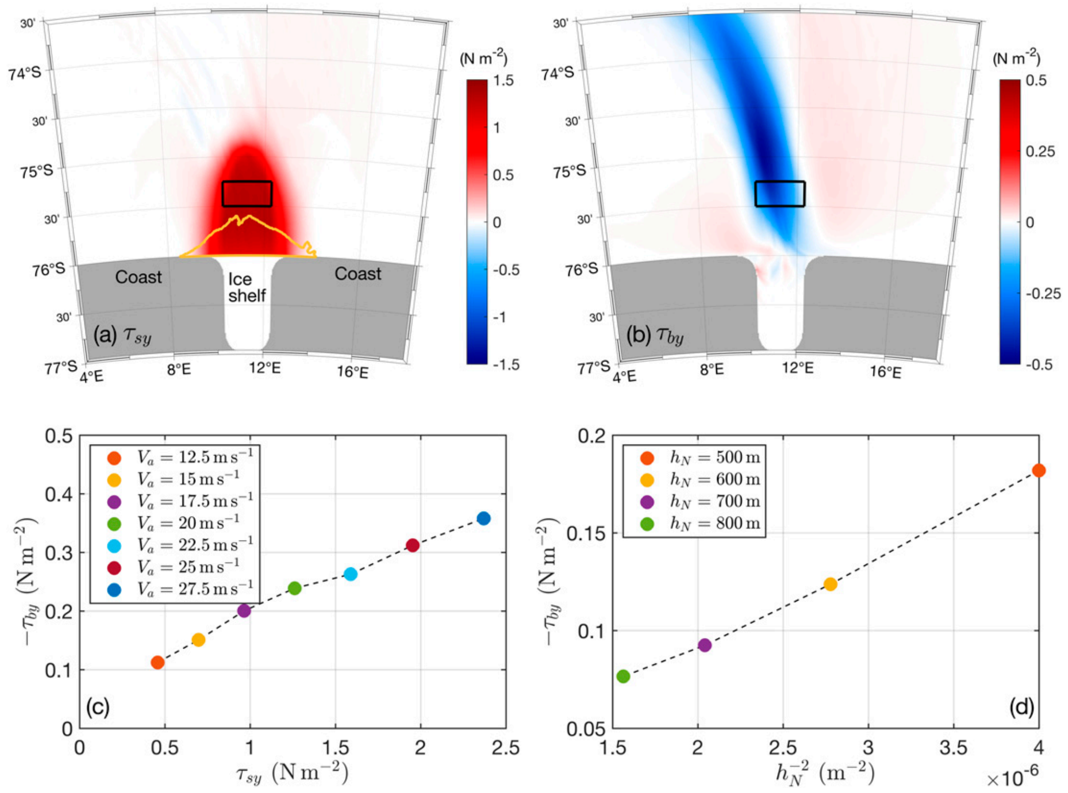

FIG. 10. Meridional stresses at the (a) surface (τ_{sy}) and (b) bottom (τ_{by}) of the ocean averaged over day 90–100 in Run B1; (c) comparison of τ_{sy} and τ_{by} averaged in the black boxes in (a) and (b); (d) τ_{by} averaged in the black boxes in (a) vs h_N^{-2} , where h_N is the water depth. The yellow line in (a) outlines the polynya.

density and maintain the mean density difference between the polynya and ambient waters. Meanwhile, $\partial\eta/\partial y$ is assumed to be independent of water depth because sea level changes are primarily induced by the wind-driven Ekman pumping in the near surface layer. Equation (2) suggests that τ_{by} is negatively related to water depth, which results from the fact that the portion of surface stress being balanced by the barotropic and baroclinic pressure gradient forces increases with water depth. This negative relation is consistent with the sensitivity simulations (G1-Hdepth) of different water depth but the same offshore ocean surface stress showing bottom stress being almost linearly related to h_N^{-2} (Fig. 10d). Here, h_N^{-2}, as an inverse function of h_N, is chosen *empirically* based on the modeled relationship between τ_{by} and h_N. The quasi-linear relationship between τ_{by} and τ_{sy} at fixed h_N and the empirical relationship between τ_{by} and h_N^{-2} at fixed V_a will be used in the scaling analysis in section 3.

To quantify the influence of different physical factors on the strength of the water column mixing in the polynya region, a metric of the mixing is needed. Here, the time it takes for the water-column stratification in the polynya region to be broken down, which we name destratification time scale (DTS), is used. The water-column stratification is considered broken down when the bottom-to-surface density difference ($\overline{\rho_{\mathrm{pb}}} - \overline{\rho_{\mathrm{ps}}}$) averaged over the polynya area reduces to $\Delta\rho_{\mathrm{MLD}} = 0.05$ kg m^{-3}. Note that this study does not aim to provide the exact time of polynya water column destratification. Rather, DTS is used to provide a convenient and objective way to compare the polynya mixing rate in different simulations and to diagnose the influence of various parameters on the mixing. For instance, time series of $\overline{\rho_{\mathrm{pb}}} - \overline{\rho_{\mathrm{ps}}}$ in B1 and B2 show dramatically different rates of reduction and, consistently, DTSs in B1 and B2 are 36 and 101 days, respectively (Fig. 11a). Comparison of the sensitivity simulations with different alongshore wind speed U_a shows that reduction rate of $\overline{\rho_{\mathrm{pb}}} - \overline{\rho_{\mathrm{ps}}}$ increases with U_a (Fig. 11b). As a result, DTS decreases with increasing U_a, meaning that polynya vertical mixing is enhanced when strong coastal easterly winds are imposed. This is consistent with the onshore Ekman transport driven by the easterly winds suppressing offshore transport of the PSW in the upper water column. Influence of the other parameters on DTS will be investigated and compared to results of the scaling analysis in section 4.

3. Analytical scaling

An analytical scale of DTS is developed here by considering the major dynamical processes in coastal polynyas. The goal is to formulate the influence of various factors (e.g., offshore wind strength, alongshore winds, air temperature, water depth, and initial ambient stratification) on water-column mixing in the polynya. Major processes in a polynya with a cross-shore width r_0 are illustrated in Fig. 12. The conditions with and without the

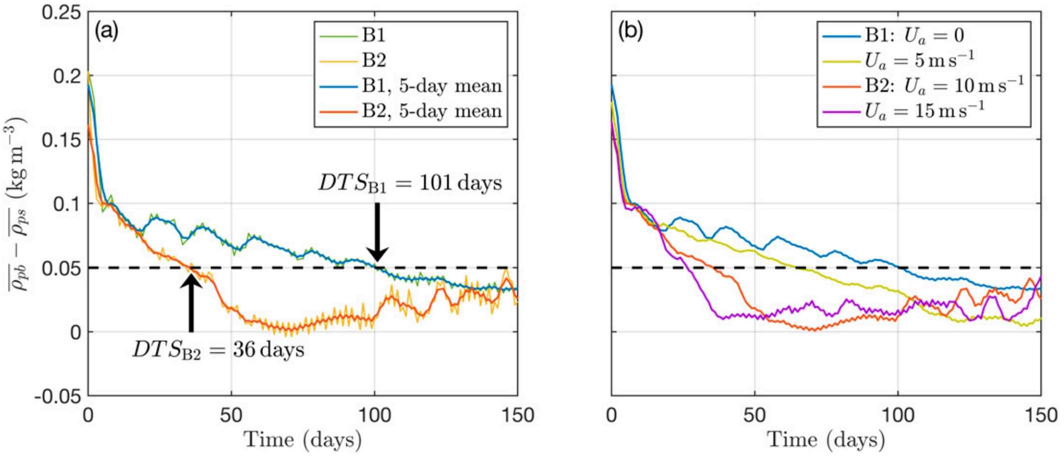

FIG. 11. (a) Daily (thin lines) and 5-day averaged (thick lines) time series of the bottom-to-surface density difference ($\overline{\rho_{\rm pb}} - \overline{\rho_{\rm ps}}$) averaged in the polynya region in Runs B1 and B2; (b) 5-day averaged time series of $\overline{\rho_{\rm pb}} - \overline{\rho_{\rm ps}}$ averaged in the polynya region for the cases of different easterly wind speed U_a. DTS is determined in each case as the time of 5-day averaged $\overline{\rho_{\rm pb}} - \overline{\rho_{\rm ps}}$ first reaching 0.05 kg m^{-3}.

coastal easterly winds are considered. Following Chapman (1999), the change of density within the polynya water column is determined by the surface buoyancy flux B_0 from buoyancy loss and the outward buoyancy flux on the sides induced by the offshore ocean current. This process can be expressed as

$$\frac{d}{dt}\iiint \rho' dA dz = \iint \frac{\rho_0 B_0}{g} dA - \int \oint \overline{v'\rho'} dl dz, \qquad (3)$$

where ρ' is the density anomaly of the water in the polynya water column relative to the ambient water, assuming that the density of the ambient water is fixed. The term A is the area of the polynya surface, z is the vertical coordinate, v' is the component of the current velocity normal to the polynya boundary, l is the length of the polynya boundary, and $\overline{v'\rho'}$ is the outward density flux at the edge of the polynya averaged both in space and time.

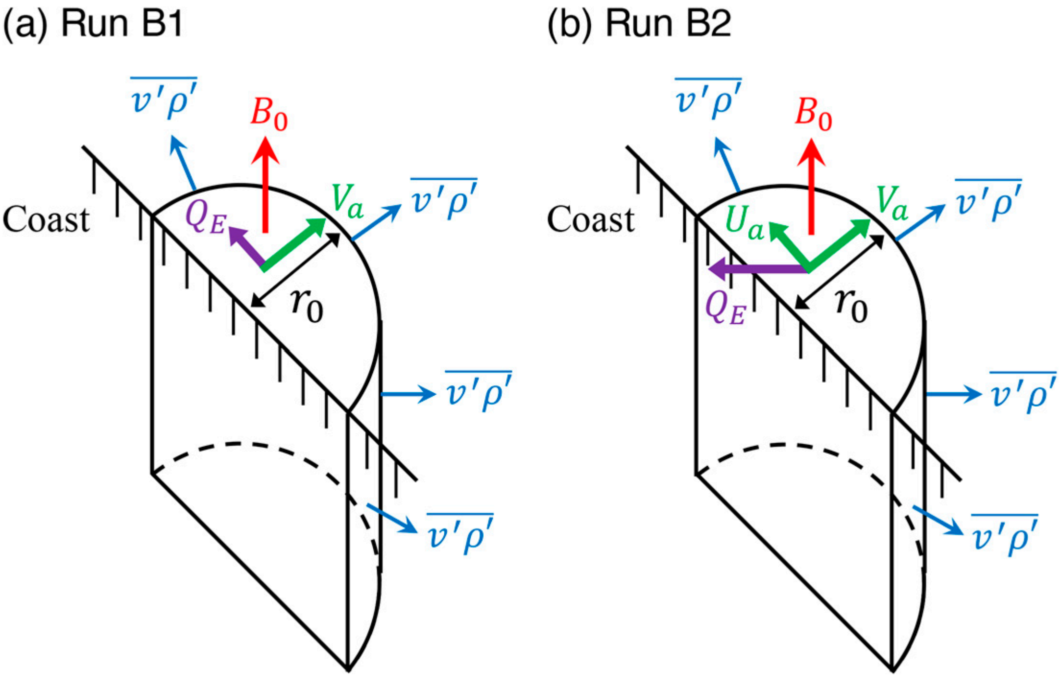

FIG. 12. Schematic illustration of the coastal polynya water column in Run (a) B1 and (b) B2 with surface buoyancy flux B_0, lateral density flux $\overline{v'\rho'}$, and polynya width r_0. The green arrows indicate the directions of offshore winds V_a and alongshore winds U_a. The purple arrows denote the direction of Ekman transport Q_E.

a. *Scaling of DTS*

As the density of the polynya surface water increases, it sinks down and erodes stratification in the polynya water column. Considering the one-dimensional downward convective penetration of a PSW plume in a linearly stratified water column and assuming no lateral spreading of the PSW, Turner (1973) gave a solution of the depth of the growing surface mixed layer (Visbeck et al. 1996):

$$h = \frac{(2Bt)^{0.5}}{N}. \tag{4}$$

Here, B is the surface buoyancy flux, t is time, and N is buoyancy frequency. A scale of the DTS, i.e., the time of the PSW plume reaching the bottom of the polynya water column with depth h_N, can thus be obtained from (4) as

$$\mathrm{DTS} = k\frac{h_N^2 N^2}{2B_e}. \tag{5}$$

Here, k is a proportionality constant between DTS and the time in (4); $N = [-(g\Delta\rho_0)/(\rho_0 h_N)]^{1/2}$ varies with the initial surface-to-bottom density difference $\Delta\rho_0$ in the polynya; B_e is the effective surface buoyancy flux, which counts only the part of the total buoyancy flux B_0 remaining in the polynya water column and excludes the rest that has been laterally carried away from the polynya region. Considering the wind-driven circulation in section 2b, B_e can be expressed as

$$B_e = B_0 - (B_t - B_c) = (1 - c)B_0. \tag{6}$$

Here, B_t is the part of the surface buoyancy flux being transported away from the polynya by the wind-driven offshore current, and is positive for outward transport across the polynya boundary; B_c is the correction term to B_t, representing the reduction of offshore transport due to any onshore flow, such as the Ekman transport driven by the coastal easterly winds; c is the ratio of total offshore transport $(B_t - B_c)$ to the surface buoyancy flux B_0. Note that the original expressions in Turner (1973) are restored when $k = 1$ and $B_t = B_c = 0$.

b. *Scaling of B_0*

When the alongshore winds are absent or weak, the total wind speed can be approximated by the offshore wind speed. Based on the thermodynamic model of a coastal polynya in Pease (1987) and Chapman (1999), considering sensible and latent heat fluxes at the surface, B_0 can be expressed as

$$B_0 = \frac{C_t g \Delta\rho_s \rho_a V_a}{L_f \rho_0 \rho_i}[C_p(T_0 - T_a) + L_e(q_0 - q_a)], \tag{7}$$

where $C_t = 2 \times 10^{-3}$ is the transfer coefficient at 2-m height for sensible and latent heat fluxes; $\Delta\rho_s$ is the density change due to brine rejection; $\rho_a = 1.3$ kg m^{-3} is the air density; $L_f = 3.34 \times 10^5$ J kg^{-1} is the latent heat of fusion of water; $\rho_i = 910$ kg m^{-3} is the density of sea ice; $C_p = 1004$ J °C^{-1} kg^{-1} is the specific heat of air; T_a and T_0 are the temperature of air at 2-m height and temperature of water at the surface of the ocean, respectively; $L_e = 2.5 \times 10^6$ J kg^{-1} is the latent heat of water evaporation; q_a is the specific humidity at 2-m height; and q_0 is the saturation specific humidity at T_0. Following the wintertime observations in the TNBP (Guest 2021a), we assume $q_a = 5 \times 10^{-4}$ in the scaling analysis and numerical model. Since the polynya surface water is nearly frozen, $T_0 = -1.8$°C, which corresponds to $q_0 = 3.3 \times 10^{-3}$. Assuming the fraction of the salt being rejected during sea ice formation is 70% (Chapman 1999), $\Delta\rho_s$ is 21 kg m^{-3}. Note that in the analytical derivations, V_a is used to represent the total wind speed in the calculations of buoyancy loss and surface stresses for simplicity. Tests with the full expression of total wind speed, $(V_a^2 + U_a^2)^{0.5}$, give negligible changes of the computed DTS (not shown).

c. *Scaling of B_t*

Using Eq. (3), the offshore transport of buoyancy flux B_t at an equilibrium state can be estimated by vertically integrating the outward density flux $\overline{v'\rho'}$ across the polynya edge,

$$\iint \frac{\rho_0 B_t}{g} dA = \int \oint_{\mathrm{out}} \overline{v'\rho'}\, dl dz. \tag{8}$$

Here, $\overline{v'\rho'}$ can be scaled as

$$\overline{v'\rho'} \sim V_0 \Delta\rho\,, \tag{9}$$

where V_0 is the mean ocean current speed, and $\Delta\rho$ is the density anomaly of the polynya water relative to the ambient water. Note that, even though the form of $\overline{v'\rho'}$ in (9) is the same as that in Chapman (1999), the transport process that (9) represents differs from that in Chapman (1999). Chapman (1999) considered only the lateral buoyancy dispersal caused by the near-bottom eddies generated by baroclinic instability of the thermal-wind-balanced density front on the polynya rim. Our analysis shows that much of the lateral buoyancy dispersal in Antarctic polynyas occurs in the upper part of the water column resulting from the offshore mean flow induced by the offshore katabatic winds. It is likely that, near the bottom, both wind-driven flows and baroclinic eddies can induce circulation and disperse the PSW. For simplicity, the scaling analysis in this study considers only the buoyancy dispersal induced by the wind-driven circulation. The density anomaly $\Delta\rho$ is assumed to be proportional to $\Delta\rho_s$, which is the density increase due to brine rejection. The V_0 is evaluated using the aforementioned quasi-linear relationship between the meridional *bottom* stress $\tau_{by} = -\rho_0 C_{D0} V_0^2$ and the meridional *surface* stress $\tau_{sy} = \rho_a C_{Da} V_a^2$, and the quasi-linear relationship between τ_{by} and h_N^{-2}. Here, $C_{D0} = 2.5 \times 10^{-3}$ is the quadratic bottom drag coefficient (Lentz 2008), τ_{sy} is dominated by the offshore meridional wind stress, C_{Da} is the air–ocean drag coefficient and, as in the numerical model, follows the expression from Large and Yeager (2004),

$$C_{Da} = \left(\frac{2.7}{V_a} + 0.142 + 0.0764 V_a\right) \times 10^{-3}. \tag{10}$$

Using the quasi-linear relationships between τ_{by} and τ_{sy} and between τ_{by} and h_N^{-2}, we obtain an expression of V_0 as

$$V_0 \sim \frac{\alpha}{h_N}\left(\frac{C_{Da}\rho_a}{C_{D0}\rho_0}\right)^{0.5} V_a. \tag{11}$$

Here, α is a constant vertical length scale introduced to maintain dimensional consistency, and its value will be determined empirically from the sensitivity simulations (section 4).

For a polynya with initially constant buoyancy frequency N, area A, and perimeter M, using Eqs. (8)–(11), Eq. (8) can be expanded as

$$\frac{\rho_0 B_t A}{g} = \alpha\left(\frac{C_{Da}\rho_a}{C_{D0}\rho_0}\right)^{0.5} V_a \Delta\rho_s M. \tag{12}$$

Rearranging Eq. (12), the offshore buoyancy flux B_t can be expressed as

$$B_t = \frac{\alpha V_a \Delta\rho_s g}{\rho_0 (A/M)}\left(\frac{C_{Da}\rho_a}{C_{D0}\rho_0}\right)^{0.5}. \tag{13}$$

d. *Scaling of B_c*

We now seek to derive a scaling formula for the onshore Ekman transport driven by the coastal easterly winds. Its influence is measured by B_c, a correction to B_t, as described in Eq. (6). Similar to Eq. (8), B_c can be obtained by vertically integrating the inward density flux across the polynya edge,

$$\frac{\rho_0 B_c}{g} A = \epsilon P \Delta\rho \int v_E dz, \tag{14}$$

where ϵ is the efficiency of the onshore lateral buoyancy flux transport induced by Ekman dynamics and accounts for the influences of factors, such as irregular polynya shape or vertically varying density anomaly, that cannot be considered explicitly in a first-order scaling analysis, v_E is the horizontal Ekman velocity. Under the coastal easterly winds of speed U_a, the net Ekman transport is $\int v_E dz = \tau_E/(\rho_0|f|)$, where $\tau_E = \rho_a C_{Da} V_a U_a$ is the westward alongshore wind stress, and f is the Coriolis frequency. Equation (14) then gives

$$B_c = \frac{\epsilon \Delta\rho_s g \rho_a C_{Da} V_a U_a}{\rho_0^2 |f| (A/M)}. \tag{15}$$

Since B_c is a reduction term to B_t, it has to satisfy $B_c \le B_t$, which set a lower bound of DTS at the extreme scenario of the onshore Ekman transport of the PSW completely balancing the offshore transport.

e. *Scaling of polynya cross-shore width r_0*

The factor, A/M, in Eqs. (13) and (15), the ratio of the polynya area and perimeter, is presumably proportional to the cross-shore width of the polynya, r_0. Following Pease (1987), under constant wind forcing, r_0 can be estimated from the balance between the wind-driven offshore advection of the sea ice (which tends to widen the polynya) and the resistance due to growth of the offshore sea ice. The expression of the maximum polynya cross-shore width can be written as (Chapman 1999),

$$r_{0\max} = \frac{\kappa V_i}{B_0}, \tag{16}$$

where $\kappa = \Delta\rho_s g h_i/\rho_0$, h_i is the collection thickness of frazil ice, and V_i is the offshore sea ice speed at the edge of the polynya, which is approximated as 3% of the offshore wind speed (Martinson and Wamser 1990). That is, $V_i \approx 0.003V_a$. Many studies have considered the parameterizations of h_i (e.g., Bauer and Martin 1983; Biggs et al. 2000; Winsor and Björk 2000) and given an average value of ~0.2 m under oscillating winds. This value is also consistent with observed thickness of consolidated ice at the edge of the TNBP (Tison et al. 2020). For simplicity, h_i is set to 0.2 m here.

For oscillating winds, if the wind period is much shorter than the ocean response time scale, the time scale of water column mixing can be assumed to be independent of the wind period (Chapman 1999), and the polynyas are persistently open with the width of $r_{0\max}$. Hence, the dependency of r_0 on the wind oscillation period P_{wind} is neglected in the scaling analysis here even though offshore winds fluctuate in reality and our numerical models. Therefore, A/M can be scaled based on (16) as

$$\frac{A}{M} \propto r_0 = \frac{0.03\kappa V_a}{B_0} = \frac{0.03\Delta\rho_s g h_i V_a}{\rho_0 B_0}. \tag{17}$$

Note that neglecting the influence of P_{wind} here results in the final scaling of DTS being independent of P_{wind}. This will be validated in section 4.

With (7) and (17), A/M and r_0 become independent of the offshore mean wind speed V_a. This is valid when V_a is high and air temperature T_a is low (Van Woert 1999). According to our numerical simulations, the offshore winds can effectively keep the polynya open when the offshore winds are in the katabatic regime with the maximum wind speed $2V_a \ge 25$ m s^{-1}. Applying Eq. (17) with the atmospheric condition used in Run B1 gives $r_0 \approx 28$ km, which is consistent with the cross-shore width of the modeled polynya (Fig. 5a).

Combining Eqs. (7), (13), (15), and (17), we obtain the coefficient c in Eq. (6) as

$$c = \frac{100}{3h_i}\left[\alpha\left(\frac{C_{Da}\rho_a}{C_{D0}\rho_0}\right)^{0.5} - \frac{\epsilon C_{Da}\rho_a U_a}{\rho_0|f|}\right]. \tag{18}$$

Equations (5)–(7) and (18) together provide a complete scaling formula for DTS:

$$\mathrm{DTS} = \frac{k\dfrac{\rho_0\rho_i}{\Delta\rho_s\rho_a}L_f h_N^2 N^2}{2C_t g V_a\left\{1 - \dfrac{100}{3h_i}\left[\alpha\left(\dfrac{C_{Da}\rho_a}{C_{D0}\rho_0}\right)^{0.5} - \dfrac{\epsilon C_{Da}\rho_a U_a}{\rho_0|f|}\right]\right\}[C_p(T_0 - T_a) + L_e(q_0 - q_a)]}\,. \tag{19}$$

Note that most of the variables in (19) are known quantities and the air–sea drag coefficient C_{Da}, is provided in (10). The independent variables, i.e., the sensitivity parameters considered in this study, are V_a, U_a, T_a, N, and h_N. There are three constant coefficients: (i) the proportionality constant between DTS and time in Turner's MLD formula, k; (ii) the vertical length scale incorporating the efficiency of the wind-driven offshore transport carrying PSW offshore, α; and (iii) the efficiency of the onshore lateral buoyancy flux transport induced by Ekman dynamics, ϵ.

Even with the simplifications we have employed in the scaling analysis, Eq. (19) remains complex and difficult to use for comparing the times required to break down the stratification in polynyas. Here, we seek to distill it to provide an intuitive understanding of the key mechanism. Recognizing (19) and combining it with (18), we obtain,

$$\mathrm{DTS} = \frac{h_N}{(1-c)[gV_a/(h_N N^2)]}\,\frac{k\dfrac{\rho_0\rho_i}{\Delta\rho_s\rho_a}L_f}{2C_t[C_p(T_0 - T_a) + L_e(q_0 - q_a)]}\,. \tag{20}$$

Considering the offshore wind speed V_a as the key forcing to produce the surface buoyancy flux that gradually erodes the stratification in the polynya water column, and neglecting the constants and other factors with relatively weak influence in (20), the DTS scaling can be simplified as

$$\mathrm{DTS} \sim \frac{h_N}{(1-c)E}\,. \tag{21}$$

Here, $E = gV_a/(h_N N^2)$ is the stratification erosion rate, which increases with increasing V_a and decreasing h_N and N. It is affected by the offshore loss and onshore compensation of the lateral buoyancy flux, which are included in the coefficient c, as shown by (18). Equation (21) is presumable applicable to gain a qualitative understanding of the key destratification processes in Antarctic coastal polynya. Overall, the scaling analysis here provides a framework for (i) investigating the influence of different factors on water column mixing in Antarctic coastal polynyas, (ii) analyzing the variability of DSW formation across different Antarctic polynyas, and (iii) understanding the temporal (e.g., interannual or longer-term) variability of stratification in a polynya, including a qualitative prediction of the future polynya mixing. For these purposes, values of the coefficients, k, α, and ϵ, need to be determined, and the depicted dynamical relationships between the physical parameters and DTS need to be validated. These are the goals of the next section.

4. Sensitivity simulations

Here, values of k, α, and ϵ, in (19) are to be determined first through fitting scaled DTS values to corresponding values given by simulations in the *calibration* sensitivity sets: G1-Vwind with variable V_a and G1-Uwind with variable U_a. Applying parameter values used in each of the 10 calibration simulations to (19) gives an expression of scaled DTS with k, α, and ϵ as dependent coefficients. Least squares fitting of the scaled DTS to the corresponding values extracted from the seven simulations in G1-Vwind gives $k = 4.49$, $\alpha = 0.138$ m, and a qualitative match between the scaled and modeled DTS (black symbols and the black dashed line in Fig. 13a); and least squares fitting to the DTS values extracted from the four simulations in G1-Uwind gives $\epsilon = 0.015$ and also a qualitative match between the scaled and modeled DTS (black symbols and the black dashed line in Fig. 13b). Because of the fittings, all 10 calibration cases together show a great match between analytically scaled and modeled DTS with an R^2 squared value of 0.96 (Fig. 14a). The validation of the scaling will be carried out below with the validation simulations.

With the fitted coefficients, the scaled DTS shows a weak quadratic-like dependence on the offshore wind speed V_a, qualitatively matching that given by simulations in G1-Vwind (Fig. 13a). The weak quadratic-like relationship results from the dependence of both the surface buoyancy flux B_0 and the air–sea drag coefficient C_{Da} on V_a, as shown in (7) and (10), respectively. In particular, under mild winds, the analytically derived DTS decreases with increasing V_a, reflecting the dominant positive influence of offshore winds on B_0 and the intensity of polynya water column mixing. When the offshore winds become much stronger, C_{Da} increases much faster, and the increase of B_t outperforms B_0. This reduces the amount of PSW remaining in the polynya region, and DTS thus increases with V_a. Therefore, within the katabatic regime considered here, the dependence of DTS on V_a is weak because of the competition between B_0 and B_t. We stress here that these differ from results of previous studies that neglect the wind-driven offshore loss of the PSW in the upper water column and consider only the direct influence of V_a on B_0. In those studies, DTS should monotonically decrease with increasing V_a.

Meanwhile, the scaled DTS shows a negative dependence on the alongshore wind speed U_a (Fig. 13b). This is consistent with stronger coastal easterly winds driving stronger onshore Ekman transport, keeping more PSW in the polynya region, and causing faster mixing of the polynya water column. This result emphasizes that wind direction can significantly change vertical mixing in Antarctic coastal polynyas. Note that to ensure $B_c \le B_t$, U_a is chosen to be no more than 15 m s^{-1} in

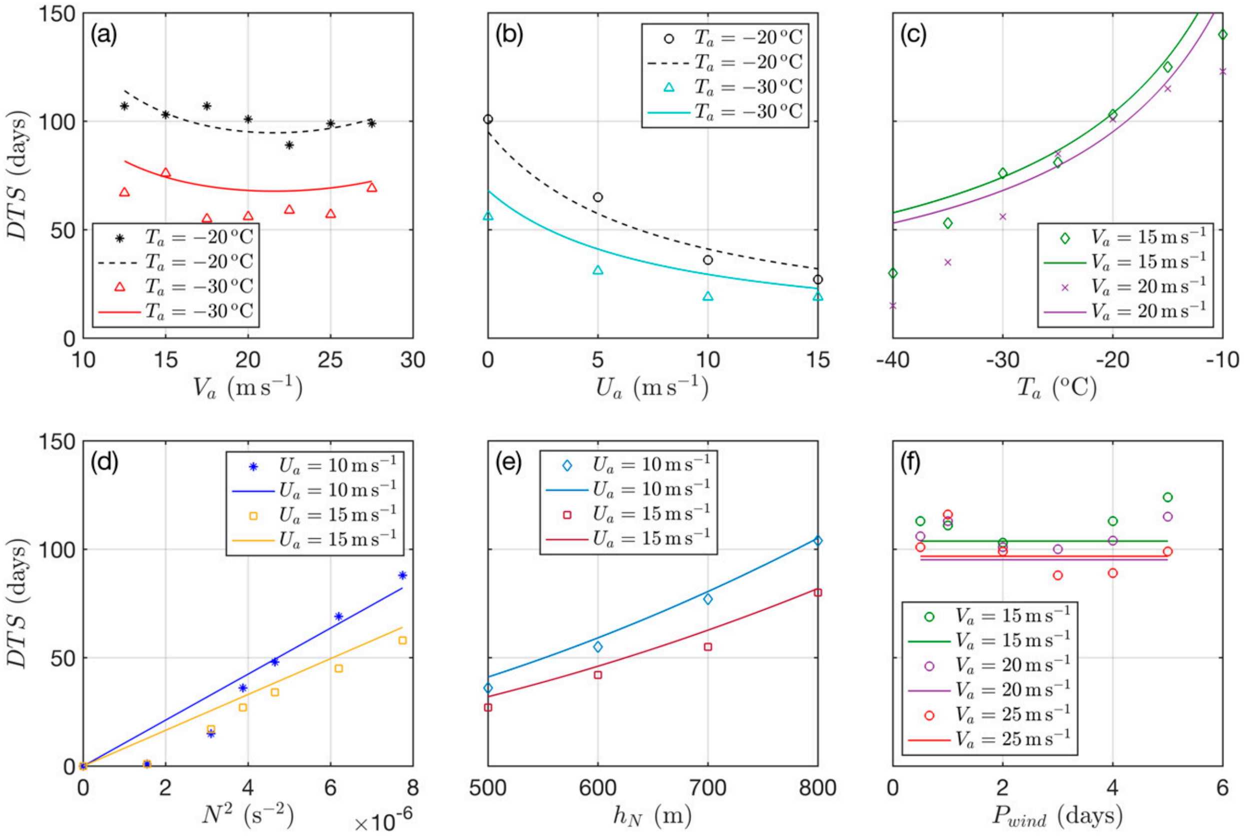

FIG. 13. Comparisons of numerically modeled DTS (symbols) and analytically derived DTS (lines) in sensitivity sets with varying values of (a) mean offshore wind speed, (b) alongshore wind speed, (c) air temperature, (d) initial ambient stratification, (e) water depth, and (f) oscillation period of the offshore winds. The black symbols in (a) and (b) are from simulations in the calibration sets (G1-Vwind and G1-Uwind) used to obtain the coefficients in the analytically scaled formulas through least squares fitting, and the black dashed lines in (a) and (b) are results of the fittings. Other symbols in (a) and (b) and all symbols in (c)–(f) are from validation sets; all solid lines are obtained from Eq. (18) with fitted coefficients and thus independent of the corresponding simulations.

both numerical and scaling analyses. This aligns with previous research showing the mean alongshore wind speed being around 10 m s^{-1} in winter over most Antarctic coastal polynyas (Nihashi and Ohshima 2015).

To validate the scaled formula, we compare scaled and modeled DTS in the 11 validation sets, including G2-Vwind and G2-Uwind, which are similar to G1-Vwind and G1-Uwind, respectively, but with air temperature, T_a, changed from the control value of −20° to −30°C (Table 2). Comparisons in all validation sets show qualitatively similar dependence of scaled and modeled DTS on the six sensitivity parameters (Fig. 13). In particular, both modeled and scaled DTS show positive dependence on T_a (Fig. 13c), reflecting the fact that, as air temperature increases, B_0 in Eq. (7) decreases with weakened buoyancy loss, and DTS increases. However, the relationship is nonlinear, and a mismatch between the scaled and modeled results remains. This is likely caused by other influencing pathways, such as air temperature affecting sea ice strength, polynya size, and then polynya mixing, being captured by the numerical model, but not considered in the analytical scaling.

Both the modeled and scaled DTS show positive dependence on the initial ambient stratification N^2 (Fig. 13d). This reflects the tendency of existing vertical stratification suppressing downward penetration of the PSW. For instance, with small N^2, PSW sinks quickly to the bottom, resulting in a small DTS. Therefore, the preconditioning of the stratification in a polynya before the winter months should be taken into account when we study polynya water column mixing. The small mismatch between the modeled and scaled dependence of DTS on N^2 at low N^2 likely results from the bottom-to-surface density difference threshold used in the modeling analysis. Because the water column is considered well mixed when the bottom-to-surface density difference in the model is smaller than 0.05 kg m^{-3}, DTS should be 0 when N^2 is lower than 10^{-6} s^{-2}, which is consistent with the trend of modeled DTS (Fig. 13d). Using a smaller density difference in the DTS definition would reduce the model-scaling mismatch at low N^2, but it would significantly increase the simulation time required for the water column to reach destratification. Because the threshold value does not affect the dynamical interpretation, 0.05 kg m^{-3} is kept here for a convenient comparison

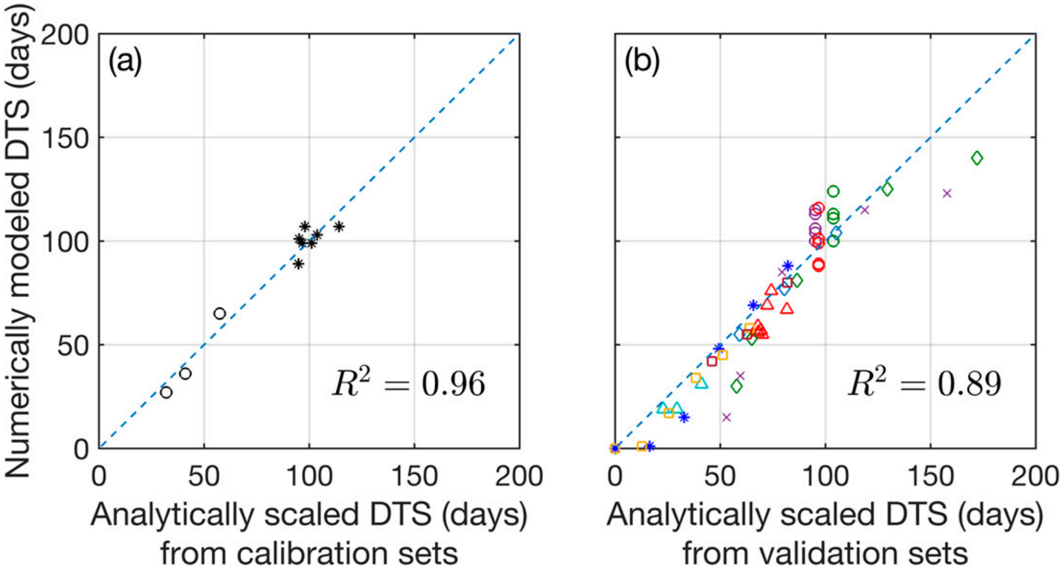

FIG. 14. Comparisons of numerically modeled and analytically scaled DTS from (a) calibration sets and (b) validation sets. The shapes of the symbols are consistent with those in Fig. 13.

among the simulations. Meanwhile, as the water depth h_N increases, both the modeled and scaled DTS increase since more time is required for the PSW to reach a deeper bottom (Fig. 13e).

Because the wind oscillation period P_{wind} is not considered in the analytical scaling, the scaled DTS does not vary with P_{wind} (Fig. 13f). Simulations in G1-Pwind, G2-Pwind, and G2-Pwindx all show weak dependence of DTS on P_{wind} with no clear trend. This is consistent with P_{wind} considered here (2–5 days) being smaller than the ocean response time scale of >10 days, as well as wind-induced high-frequency oscillations of $\overline{\rho_{\mathrm{pb}}} - \overline{\rho_{\mathrm{ps}}}$ being relatively small (Fig. 11a). It is likely that wind oscillation of longer periods will have a more pronounced influence on the polynya water-column mixing, which is not addressed here.

We have also considered the influence of Coriolis parameter f by moving the model domain southward by 10° latitude, which covers the latitude range of most Antarctic coastal polynyas. These simulations (not shown) give very similar results as B1 and B2. This is not surprising because f changes only 6% with the 10° latitude shift. Because both f and U_a affect DTS through the onshore Ekman transport and they appear together in (19), the influence of f can directly be compared to that of U_a. Simulations in G1-Uwind and G2-Uwind show that changing U_a by 6%, i.e., 0.6 m s^{-1}, has negligible impact on DTS (Fig. 13b).

Combining all 11 validation sets together, the scaled DTS shows a general alignment with the model results with a R^2 squared value of 0.89 (Fig. 14b). This alignment with the output of the independent validation simulations confirms that the scaling analysis captures the major dynamical processes of the modeled polynyas and demonstrates that the scaled formula can be used to qualitatively examine the influence of the considered parameters on the polynya mixing.

5. Discussion

Considering the influence of winds, sea ice, and ice shelf, this study demonstrates that water column mixing and PSW formation in Antarctic coastal polynyas, as well as intrusion of the PSW into the neighboring ice shelf cavity are directly impacted by three-dimensional ocean circulation in the polynya region. Offshore transport of the PSW in the upper part of the water column induced by the katabatic offshore winds can be a major loss of the PSW in the polynya and substantially reduce the strength of the local vertical mixing. Meanwhile, through generating onshore Ekman transport, the prominent coastal easterly winds along the Antarctic coast could suppress lateral loss of the buoyancy flux toward the offshore and enhance vertical mixing in the polynya region. Note that because the conditions considered here are highly simplified, the absolute values of the DTS obtained here cannot be directly applied to any particular Antarctic coastal polynya. Moreover, while the scalings of the surface buoyancy loss and the onshore Ekman transport are based on fundamental physics, the derivation of the offshore transport relies on an empirical relationship between the surface stress and water depth, which may not necessarily be applicable to all situations. However, as the parameter space considered here is representative of many Antarctic coastal polynyas, the captured dynamics and parameter dependences are robust. For instance, observations in both the Cape Darnley Polynya (Ohshima et al. 2013) and Mertz Polynya (Martin et al. 2017; Snow et al. 2016) show flow directions of the DSW being aligned with the northwestward offshore winds, which is consistent with our model result.

This work emphasizes the impact of wind-driven ocean current on the PSW transport and destratification process. It stresses the importance of considering the influence of winds and sea ice when studying polynya dynamics. This is missing in previous studies of polynya dynamics (e.g., Årthun et al. 2013; Chapman and Gawarkiewicz 1997; Chapman 1998, 1999; Visbeck et al. 1996; Wilchinsky and Feltham 2008; Zhang and Cenedese 2014) where the sea ice dynamics and air–sea momentum transfer are neglected.

Circulations in real Antarctic coastal polynyas are complex and also affected by other factors, such as variable offshore and upstream conditions, irregular seafloor bathymetry (e.g., troughs, depressions and banks), frazil ice, ice tongues, icebergs, and complex coastlines, which are not considered in this study. For instance, studies have demonstrated that troughs on the Antarctic shelf can facilitate intrusion of the Circumpolar Deep Water toward the Antarctic coast (e.g., St-Laurent et al. 2013), and depressions on the shelf could accumulate the PSW (e.g., Williams et al. 2008). Frazil ice formation has been shown as an important component in the DSW formation in polynyas (Ohshima et al. 2022). All of these could potentially modify the stratification in the coastal polynyas. Moreover, ambient shelf and slope circulation could also affect the polynya flows and PSW dispersal pattern. For instance, because polynyas on the eastern Antarctic coast are adjacent to the shelf break (Tamura et al. 2016), the Antarctic Slope Current (Stewart et al. 2019) may affect the zonal transport of the PSW. Therefore, to understand the water column mixing in a specific polynya would require investigation of the influence of all these factors as well. Moving toward that direction and also motivated by the condition at the TNBP, Part II of this study will examine how a neighboring ice tongue and a nearby headland can modify polynya circulation and mixing.

6. Summary

This study examines the dynamics of various physical factors influencing wintertime PSW formation and water column mixing in Antarctic coastal polynyas. This Part I work combines process-oriented idealized simulations and dynamical scaling analysis, to investigate the influence of offshore winds, alongshore winds, air temperature, initial stratification, and water depth on the polynya destratification time scales. The time required to destratify the polynya water column, the destratification time scale (DTS), is chosen to represent the strength of polynya water column mixing as it is directly related to the potential of DSW production in a polynya within a winter. The idealized polynya configurations considered here represent typical conditions of some Antarctic coastal polynyas. The numerical simulations qualitatively capture fundamental hydrographic and sea ice processes in polynya regions depicted by satellite images and in situ observations. The model simulations show that much of the PSW is directly transported offshore by the wind-driven offshore flow and does not contribute to vertical mixing in the polynya water column (Figs. 5 and 6). Meanwhile, onshore Ekman transport induced by the alongshore easterly winds, a common feature of many Antarctic coastal regions, can suppress the offshore loss of the PSW and enhance vertical mixing in coastal polynyas (Figs. 6 and 7). These suggest that the polynya water column mixing is directly affected by three-dimensional circulation in the polynya region and that including the effects of both katabatic and alongshore winds is necessary for capturing characteristics of the polynya mixing.

To synthesize the influence of the physical factors, analytical scaling of polynya destratification time scales is performed (section 3). The derived formula, Eq. (19), is validated against numerical sensitivity simulations (section 4). General agreement between the scaled and modeled DTS confirms that the scaling analysis capture fundamental dynamics of the coastal polynyas (Figs. 13 and 14), including dependence of the destratification time scale on a number of physical factors: (i) stronger offshore katabatic winds can both *enhance* the polynya mixing through generating more PSW and *suppress* the mixing through transport more PSW offshore at the same time, which results in a nonlinear relationship between DTS and the offshore wind speed; (ii) typical period of offshore wind oscillation has little impact on the polynya mixing because it is shorter than the ocean response time scale; (iii) stronger coastal easterly winds drive stronger onshore Ekman transport, cause weaker offshore loss of the PSW, and result in faster destratification of the polynya water column; (iv) higher air temperature reduces the sea ice and PSW formation, and then weakens polynya mixing; and (v) stronger initial stratification of the water column suppresses mixing and slows down polynya destratification.

The process-oriented simulations, the derived scaling formula, and the dynamical relationships presented in this study provide a framework to investigate the influence of other physical factors on water column mixing in Antarctic coastal polynyas, to compare the DSW formation in different polynyas, and to understand temporal evolution of PSW formation in a polynya for given large-scale environmental changes. Moving toward that direction, Part II of this study will investigate the influence of an ice tongue and headland on the polynya mixing. Future studies should analyze the influence of other factors, such as bathymetry and upstream conditions. These studies together would provide a path toward parameterization of polynya processes in large-scale, low-resolution models that cannot explicitly resolve small-scale polynya processes.

Acknowledgments. This study is supported by the National Science Foundation through Grants OPP-1643735, OPP-1643901, and OPP-2021245. YX and WGZ are also supported by OPP-2205008.

Data availability statement. The MODIS image was obtained from the Worldview tool from NASA's Earth Observing System Data and Information System at https://worldview.earthdata.nasa.gov/. The Sentinel-1 image processed by ESA was downloaded from NASA's Distributed Active Archive Centers operated by the Alaska Satellite Facility at https://asf.alaska.edu/. The marine mammal data were collected and made freely available at http://www.meop.net by the International MEOP Consortium and the national programs that contribute to it. The meteorological station data were obtained from the Australian Antarctic Data Center at https://data.aad.gov.au/metadata/records/Antarctic_Meteorology. The model code and scripts used to conduct the simulations and analyses in this study are available at https://doi.org/10.5281/zenodo.7735630.

REFERENCES

Adolphs, U., and G. Wendler, 1995: A pilot study on the interactions between katabatic winds and polynyas at the Adélie coast, eastern Antarctica. *Antarct. Sci.*, **7**, 307–314, https://doi.org/10.1017/S0954102095000423.

Aoki, S., K. Ono, D. Hirano, and T. Tamura, 2020: Continuous winter oceanic profiling in the Cape Darnley polynya, East Antarctica. *J. Oceanogr.*, **76**, 365–372, https://doi.org/10.1007/s10872-020-00550-w.

Arrigo, K. R., and G. L. van Dijken, 2003: Phytoplankton dynamics within 37 Antarctic coastal polynya systems. *J. Geophys. Res.*, **108**, 3271, https://doi.org/10.1029/2002JC001739.

Årthun, M., P. R. Holland, K. W. Nicholls, and D. L. Feltham, 2013: Eddy-driven exchange between the open ocean and a sub–ice shelf cavity. *J. Phys. Oceanogr.*, **43**, 2372–2387, https://doi.org/10.1175/JPO-D-13-0137.1.

Barnes-Keoghan, I., 2000: Antarctic climate data collected by Australian agencies, version 1. Australian Antarctic Data Centre, accessed 2 May 2021, https://data.aad.gov.au/metadata/records/Antarctic_Meteorology.

Bauer, J., and S. Martin, 1983: A model of grease ice growth in small leads. *J. Geophys. Res.*, **88**, 2917–2925, https://doi.org/10.1029/JC088iC05p02917.

Biggs, N. R. T., M. A. Morales Maqueda, and A. J. Willmott, 2000: Polynya flux model solutions incorporating a parameterization for the collection thickness of consolidated new ice. *J. Fluid Mech.*, **408**, 179–204, https://doi.org/10.1017/S0022112099007673.

Chapman, D. C., 1998: Setting the scales of the ocean response to isolated convection. *J. Phys. Oceanogr.*, **28**, 606–620, https://doi.org/10.1175/1520-0485(1998)028<0606:STSOTO>2.0.CO;2.

——, 1999: Dense water formation beneath a time-dependent coastal polynya. *J. Phys. Oceanogr.*, **29**, 807–820, https://doi.org/10.1175/1520-0485(1999)029<0807:DWFBAT>2.0.CO;2.

——, and G. Gawarkiewicz, 1997: Shallow convection and buoyancy equilibration in an idealized coastal polynya. *J. Phys. Oceanogr.*, **27**, 555–566, https://doi.org/10.1175/1520-0485(1997)027<0555:SCABEI>2.0.CO;2.

Dai, L., H. Xie, S. F. Ackley, and A. M. Mestas-Nuñez, 2020: Ice production in Ross Ice Shelf polynyas during 2017–2018 from Sentinel-1 SAR images. *Remote Sens.*, **12**, 1484, https://doi.org/10.3390/rs12091484.

Davis, A. M. J., and R. T. McNider, 1997: The development of Antarctic katabatic winds and implications for the coastal ocean. *J. Atmos. Sci.*, **54**, 1248–1261, https://doi.org/10.1175/1520-0469(1997)054<1248:TDOAKW>2.0.CO;2.

Ding, Y., X. Cheng, X. Li, M. Shokr, J. Yuan, Q. Yang, and F. Hui, 2020: Specific relationship between the surface air temperature and the area of the Terra Nova Bay polynya, Antarctica. *Adv. Atmos. Sci.*, **37**, 532–544, https://doi.org/10.1007/s00376-020-9146-2.

Dong, S., J. Sprintall, S. T. Gille, and L. Talley, 2008: Southern Ocean mixed-layer depth from Argo float profiles. *J. Geophys. Res.*, **113**, C06013, https://doi.org/10.1029/2006JC004051.

Ekman, V. W., 1905: On the influence of the Earth's rotation on ocean-currents. *Ark. Mat. Astron. Fys.*, **2**, 1–53.

Guest, P. S., 2021a: Inside katabatic winds over the Terra Nova Bay polynya: 1. Atmospheric jet and surface conditions. *J. Geophys. Res. Atmos.*, **126**, e2021JD034902, https://doi.org/10.1029/2021JD034902.

——, 2021b: Inside katabatic winds over the Terra Nova Bay polynya: 2. Dynamic and thermodynamic analyses. *J. Geophys. Res. Atmos.*, **126**, e2021JD034904, https://doi.org/10.1029/2021JD034904.

Hellmer, H. H., and D. J. Olbers, 1989: A two-dimensional model for the thermohaline circulation under an ice shelf. *Antarct. Sci.*, **1**, 325–336, https://doi.org/10.1017/S0954102089000490.

Hibler, W. D., III, 1979: A dynamic thermodynamic sea ice model. *J. Phys. Oceanogr.*, **9**, 815–846, https://doi.org/10.1175/1520-0485(1979)009<0815:ADTSIM>2.0.CO;2.

Jacobs, S. S., A. F. Amos, and P. M. Bruchhausen, 1970: Ross Sea oceanography and Antarctic Bottom Water formation. *Deep-Sea Res. Oceanogr. Abstr.*, **17**, 935–962, https://doi.org/10.1016/0011-7471(70)90046-X.

Jenkins, A., H. H. Hellmer, and D. M. Holland, 2001: The role of meltwater advection in the formulation of conservative boundary conditions at an ice–ocean interface. *J. Phys. Oceanogr.*, **31**, 285–296, https://doi.org/10.1175/1520-0485(2001)031<0285:TROMAI>2.0.CO;2.

Kitade, Y., and Coauthors, 2014: Antarctic bottom water production from the Vincennes Bay Polynya, East Antarctica. *Geophys. Res. Lett.*, **41**, 3528–3534, https://doi.org/10.1002/2014GL059971.

Knuth, S. L., and J. J. Cassano, 2011: An analysis of near-surface winds, air temperature, and cyclone activity in Terra Nova Bay, Antarctica, from 1993 to 2009. *J. Appl. Meteor. Climatol.*, **50**, 662–680, https://doi.org/10.1175/2010JAMC2507.1.

Kusahara, K., G. D. Williams, T. Tamura, R. Massom, and H. Hasumi, 2017: Dense shelf water spreading from Antarctic coastal polynyas to the deep Southern Ocean: A regional circumpolar model study. *J. Geophys. Res. Oceans*, **122**, 6238–6253, https://doi.org/10.1002/2017JC012911.

Large, W. G., and S. G. Yeager, 2004: Diurnal to decadal global forcing for ocean and sea-ice models: The data sets and flux climatologies. NCAR Tech. Note NCAR/TN-460+STR, 105 pp., https://doi.org/10.5065/D6KK98Q6.

——, J. C. McWilliams, and S. C. Doney, 1994: Oceanic vertical mixing: A review and a model with a nonlocal boundary layer parameterization. *Rev. Geophys.*, **32**, 363–403, https://doi.org/10.1029/94RG01872.

Le Bel, D. A., C. J. Zappa, G. Budillon, and A. L. Gordon, 2021: Salinity response to atmospheric forcing of the Terra Nova Bay polynya, Antarctica. *Antarct. Sci.*, **33**, 318–331, https://doi.org/10.1017/S0954102021000146.

Lentz, S. J., 2008: Seasonal variations in the circulation over the Middle Atlantic Bight continental shelf. *J. Phys. Oceanogr.*, **38**, 1486–1500, https://doi.org/10.1175/2007JPO3767.1.

Li, Y., R. Ji, S. Jenouvrier, M. Jin, and J. Stroeve, 2016: Synchronicity between ice retreat and phytoplankton bloom in circum-Antarctic polynyas. *Geophys. Res. Lett.*, **43**, 2086–2093, https://doi.org/10.1002/2016GL067937.

Lipscomb, W. H., E. C. Hunke, W. Maslowski, and J. Jakacki, 2007: Ridging, strength, and stability in high-resolution sea ice models. *J. Geophys. Res.*, **112**, C03S91, https://doi.org/10.1029/2005JC003355.

Losch, M., 2008: Modeling ice shelf cavities in a *z* coordinate ocean general circulation model. *J. Geophys. Res.*, **113**, C08043, https://doi.org/10.1029/2007JC004368.

——, D. Menemenlis, J.-M. Campin, P. Heimbach, and C. Hill, 2010: On the formulation of sea-ice models. Part 1: Effects of different solver implementations and parameterizations. *Ocean Modell.*, **33**, 129–144, https://doi.org/10.1016/j.ocemod.2009.12.008.

Marshall, J., A. Adcroft, C. Hill, L. Perelman, and C. Heisey, 1997: A finite-volume, incompressible Navier Stokes model for, studies of the ocean on parallel computers. *J. Geophys. Res.*, **102**, 5753–5766, https://doi.org/10.1029/96JC02775.

Martin, A., M. N. Houssais, H. Le Goff, C. Marec, and D. Dausse, 2017: Circulation and water mass transports on the East Antarctic shelf in the Mertz Glacier region. *Deep-Sea Res. I*, **126**, 1–20, https://doi.org/10.1016/j.dsr.2017.05.007.

Martinson, D. G., and C. Wamser, 1990: Ice drift and momentum exchange in winter Antarctic pack ice. *J. Geophys. Res.*, **95**, 1741–1755, https://doi.org/10.1029/JC095iC02p01741.

Mathiot, P., B. Barnier, H. Gallée, J. M. Molines, J. Le Sommer, M. Juza, and T. Penduff, 2010: Introducing katabatic winds in global ERA40 fields to simulate their impacts on the Southern Ocean and sea-ice. *Ocean Modell.*, **35**, 146–160, https://doi.org/10.1016/j.ocemod.2010.07.001.

——, N. C. Jourdain, B. Barnier, H. Gallée, J. M. Molines, J. Le Sommer, and T. Penduff, 2012: Sensitivity of coastal polynyas and high-salinity shelf water production in the Ross Sea, Antarctica, to the atmospheric forcing. *Ocean Dyn.*, **62**, 701–723, https://doi.org/10.1007/s10236-012-0531-y.

Meehl, G. A., J. M. Arblaster, C. T. Y. Chung, M. M. Holland, A. DuVivier, L. A. Thompson, D. Yang, and C. M. Bitz, 2019: Sustained ocean changes contributed to sudden Antarctic sea ice retreat in late 2016. *Nat. Commun.*, **10**, 14 https://doi.org/10.1038/s41467-018-07865-9.

Morales Maqueda, M. A., A. J. Willmott, and N. R. T. Biggs, 2004: Polynya dynamics: A review of observations and modeling. *Rev. Geophys.*, **42**, RG1004, https://doi.org/10.1029/2002RG000116.

Nakayama, Y., D. Menemenlis, M. Schodlok, and E. Rignot, 2017: Amundsen and Bellingshausen Seas simulation with optimized ocean, sea ice, and thermodynamic ice shelf model parameters. *J. Geophys. Res. Oceans*, **122**, 6180–6195, https://doi.org/10.1002/2016JC012538.

——, and Coauthors, 2019: Pathways of ocean heat towards Pine Island and Thwaites grounding lines. *Sci. Rep.*, **9**, 16649, https://doi.org/10.1038/s41598-019-53190-6.

Nguyen, A. T., D. Menemenlis, and R. Kwok, 2011: Arctic ice-ocean simulation with optimized model parameters: Approach and assessment. *J. Geophys. Res.*, **116**, C04025, https://doi.org/10.1029/2010JC006573.

Nihashi, S., and K. I. Ohshima, 2015: Circumpolar mapping of Antarctic coastal polynyas and landfast sea ice: Relationship and variability. *J. Climate*, **28**, 3650–3670, https://doi.org/10.1175/JCLI-D-14-00369.1.

Ohshima, K. I., and Coauthors, 2013: Antarctic Bottom Water production by intense sea-ice formation in the Cape Darnley polynya. *Nat. Geosci.*, **6**, 235–240, https://doi.org/10.1038/ngeo1738.

——, and Coauthors, 2022: Dominant frazil ice production in the Cape Darnley polynya leading to Antarctic Bottom Water formation. *Sci. Adv.*, **8**, eadc9174, https://doi.org/10.1126/sciadv.adc9174.

Orlanski, I., 1976: A simple boundary condition for unbounded hyperbolic flows. *J. Comput. Phys.*, **21**, 251–269, https://doi.org/10.1016/0021-9991(76)90023-1.

Parish, T. R., and D. H. Bromwich, 2007: Reexamination of the near-surface airflow over the Antarctic continent and implications on atmospheric circulations at high southern latitudes. *Mon. Wea. Rev.*, **135**, 1961–1973, https://doi.org/10.1175/MWR3374.1.

Parmiggiani, F., 2006: Fluctuations of Terra Nova Bay polynya as observed by active (ASAR) and passive (AMSR-E) microwave radiometers. *Int. J. Remote Sens.*, **27**, 2459–2467, https://doi.org/10.1080/01431160600554355.

Pease, C. H., 1987: The size of wind-driven coastal polynyas. *J. Geophys. Res.*, **92**, 7049–7059, https://doi.org/10.1029/JC092iC07p07049.

Rocha, C. B., T. K. Chereskin, S. T. Gille, and D. Menemenlis, 2016: Mesoscale to submesoscale wavenumber spectra in Drake Passage. *J. Phys. Oceanogr.*, **46**, 601–620, https://doi.org/10.1175/JPO-D-15-0087.1.

Roquet, F., and Coauthors, 2014: A Southern Indian Ocean database of hydrographic profiles obtained with instrumented elephant seals. *Sci. Data*, **1**, 140028, https://doi.org/10.1038/sdata.2014.28.

——, and Coauthors, 2021: MEOP-CTD in-situ data collection: A Southern Ocean marine-mammals calibrated sea water temperatures and salinities observations. SEANOE, accessed 7 December 2021, https://doi.org/10.17882/45461.

Rusciano, E., G. Budillon, G. Fusco, and G. Spezie, 2013: Evidence of atmosphere-sea ice-ocean coupling in the Terra Nova Bay polynya (Ross Sea-Antarctica). *Cont. Shelf Res.*, **61–62**, 112–124, https://doi.org/10.1016/j.csr.2013.04.002.

Schmidtko, S., K. J. Heywood, A. F. Thompson, and S. Aoki, 2014: Multidecadal warming of Antarctic waters. *Science*, **346**, 1227–1231, https://doi.org/10.1126/science.1256117.

Schultz, C., S. C. Doney, W. G. Zhang, H. Regan, P. Holland, M. P. Meredith, and S. Stammerjohn, 2020: Modeling of the influence of sea ice cycle and Langmuir circulation on the upper ocean mixed layer depth and freshwater distribution at the West Antarctic Peninsula. *J. Geophys. Res. Oceans*, **125**, e2020JC016109, https://doi.org/10.1029/2020JC016109.

Silvano, A., S. R. Rintoul, B. Peña-Molino, W. R. Hobbs, E. Van Wijk, S. Aoki, T. Tamura, and G. D. Williams, 2018: Freshening by glacial meltwater enhances melting of ice shelves and reduces formation of Antarctic Bottom Water. *Sci. Adv.*, **4**, eaap9467, https://doi.org/10.1126/sciadv.aap9467.

Smagorinsky, J., 1963: General circulation experiments with the primitive equations. *Mon. Wea. Rev.*, **91**, 99–164, https://doi.org/10.1175/1520-0493(1963)091<0099:GCEWTP>2.3.CO;2.

Smith, W. O., Jr., and D. G. Barber, Eds., 2007: *Polynyas: Windows to the World*. Elsevier, 474 pp.

Snow, K., B. M. Sloyan, S. R. Rintoul, A. M. Hogg, and S. M. Downes, 2016: Controls on circulation, cross-shelf exchange, and dense water formation in an Antarctic polynya. *Geophys. Res. Lett.*, **43**, 7089–7096, https://doi.org/10.1002/2016GL069479.

Stewart, A. L., A. Klocker, and D. Menemenlis, 2019: Acceleration and overturning of the Antarctic Slope Current by winds, eddies, and tides. *J. Phys. Oceanogr.*, **49**, 2043–2074, https://doi.org/10.1175/JPO-D-18-0221.1.

St-Laurent, P., J. M. Klinck, and M. S. Dinniman, 2013: On the role of coastal troughs in the circulation of warm Circumpolar Deep Water on Antarctic shelves. *J. Phys. Oceanogr.*, **43**, 51–64, https://doi.org/10.1175/JPO-D-11-0237.1.

Tamura, T., K. I. Ohshima, and S. Nihashi, 2008: Mapping of sea ice production for Antarctic coastal polynyas. *Geophys. Res. Lett.*, **35**, L07606, https://doi.org/10.1029/2007GL032903.

——, ——, A. D. Fraser, and G. D. Williams, 2016: Sea ice production variability in Antarctic coastal polynyas. *J. Geophys. Res. Oceans*, **121**, 2967–2979, https://doi.org/10.1002/2015JC011537.

Thorndike, A. S., D. A. Rothrock, G. A. Maykut, and R. Colony, 1975: The thickness distribution of sea ice. *J. Geophys. Res.*, **80**, 4501–4513, https://doi.org/10.1029/JC080i033p04501.

Tison, J.-L., and Coauthors, 2020: Physical and biological properties of early winter Antarctic sea ice in the Ross Sea. *Ann. Glaciol.*, **61**, 241–259, https://doi.org/10.1017/aog.2020.43.

Turner, J. S., 1973: *Buoyancy Effects in Fluids*. Cambridge University Press, 367 pp.

Van Woert, M. L., 1999: Wintertime dynamics of the Terra Nova Bay polynya. *J. Geophys. Res.*, **104**, 7753–7769, https://doi.org/10.1029/1999JC900003.

Visbeck, M., J. Marshall, and H. Jones, 1996: Dynamics of isolated convective regions in the ocean. *J. Phys. Oceanogr.*, **26**, 1721–1734, https://doi.org/10.1175/1520-0485(1996)026<1721:DOICRI>2.0.CO;2.

Wendler, G., D. Gilmore, and J. Curtis, 1997: On the formation of coastal polynyas in the area of Commonwealth Bay, eastern Antarctica. *Atmos. Res.*, **45**, 55–75, https://doi.org/10.1016/S0169-8095(97)00024-0.

Wenta, M., and J. J. Cassano, 2020: The atmospheric boundary layer and surface conditions during katabatic wind events over the Terra Nova Bay polynya. *Remote Sens.*, **12**, 4160, https://doi.org/10.3390/rs12244160.

Wilchinsky, A. V., and D. L. Feltham, 2008: Generation of a buoyancy-driven coastal current by an Antarctic polynya. *J. Phys. Oceanogr.*, **38**, 1011–1032, https://doi.org/10.1175/2007JPO3831.1.

Williams, G. D., and N. L. Bindoff, 2003: Wintertime oceanography of the Adélie depression. *Deep-Sea Res. II.*, **50**, 1373–1392, https://doi.org/10.1016/S0967-0645(03)00074-2.

——, ——, S. J. Marsland, and S. R. Rintoul, 2008: Formation and export of dense shelf water from the Adélie depression, East Antarctica. *J. Geophys. Res.*, **113**, C04039, https://doi.org/10.1029/2007JC004346.

——, S. Aoki, S. S. Jacobs, S. R. Rintoul, T. Tamura, and N. L. Bindoff, 2010: Antarctic bottom water from the Adélie and George v Land Coast, East Antarctica (140°–149°E). *J. Geophys. Res.*, **115**, C04027, https://doi.org/10.1029/2009JC005812.

Winsor, P., and G. Björk, 2000: Polynya activity in the Arctic Ocean from 1958 to 1997. *J. Geophys. Res.*, **105**, 8789–8803, https://doi.org/10.1029/1999JC900305.

Xu, Y., W. G. Zhang, T. Maksym, R. Ji, and Y. Li, 2023: Stratification breakdown in Antarctic coastal polynyas. Part II: Influence of an ice tongue and coastline geometry. *J. Phys. Oceonogr.*, **53**, 2069–2088, https://doi.org/10.1175/JPO-D-22-0219.1.

Zhang, J., and W. D. Hibler III, 1997: On an efficient numerical method for modeling sea ice dynamics. *J. Geophys. Res.*, **102**, 8691–8702, https://doi.org/10.1029/96JC03744.

Zhang, W. G., and C. Cenedese, 2014: The dispersal of dense water formed in an idealized coastal polynya on a shallow sloping shelf. *J. Phys. Oceanogr.*, **44**, 1563–1581, https://doi.org/10.1175/JPO-D-13-0188.1.